Published in final edited form as:
J Nucl Med. 2010 May 1; 51(0 1): 3S–17S. doi:10.2967/jnumed.109.068130.

Design of Targeted Cardiovascular Molecular Imaging Probes

Carolyn J. Anderson[1], **Jeff W.M. Bulte**[2], **Kai Chen**[3], **Xiaoyuan Chen**[3], **Ban-An Khaw**[4], **Monica Shokeen**[1], **Karen L. Wooley**[5,6], and **Henry F. VanBrocklin**[7]

[1]Mallinckrodt Institute of Radiology, School of Medicine, Washington University, St. Louis, Missouri [2]Russell H. Morgan, Department of Radiology and Radiological Science, School of Medicine, The Johns Hopkins University, Baltimore, Maryland [3]National Institute of Biomedical Imaging and Biomedical Engineering, National Institutes of Health, Bethesda, Maryland [4]Department of Pharmaceutical Sciences, Bouvé College of Health Sciences, Northeastern University, Boston, Massachusetts [5]Department of Chemistry, Texas A&M University, College Station, Texas [6]Department of Chemical Engineering, Texas A&M University, College Station, Texas [7]Department of Radiology and Biomedical Imaging, University of California, San Francisco, San Francisco, California

Abstract

Molecular imaging relies on the development of sensitive and specific probes coupled with imaging hardware and software to provide information about the molecular status of a disease and its response to therapy, which are important aspects of disease management. As genomic and proteomic information from a variety of cardiovascular diseases becomes available, new cellular and molecular targets will provide an imaging readout of fundamental disease processes. A review of the development and application of several cardiovascular probes is presented here. Strategies for labeling cells with superparamagnetic iron oxide nanoparticles enable monitoring of the delivery of stem cell therapies. Small molecules and biologics (e.g., proteins and antibodies) with high affinity and specificity for cell surface receptors or cellular proteins as well as enzyme substrates or inhibitors may be labeled with single-photon–emitting or positron-emitting isotopes for nuclear molecular imaging applications. Labeling of bispecific antibodies with single-photon–emitting isotopes coupled with a pretargeting strategy may be used to enhance signal accumulation in small lesions. Emerging nanomaterials will provide platforms that have various sizes and structures and that may be used to develop multimeric, multimodal molecular imaging agents to probe one or more targets simultaneously. These platforms may be chemically manipulated to afford molecules with specific targeting and clearance properties. These examples of molecular imaging probes are characteristic of the multidisciplinary nature of the extraction of advanced biochemical information that will enhance diagnostic evaluation and drug development and predict clinical outcomes, fulfilling the promise of personalized medicine and improved patient care.

Keywords

molecular imaging; bispecific antibodies; multimeric molecular imaging agents; nanomaterials; superparamagnetic iron oxide; nanoparticles

For correspondence or reprints contact: Henry F. VanBrocklin, Department of Radiology and Biomedical Imaging, University of California, San Francisco, 185 Berry St., Suite 350, San Francisco, CA 94107..

The application of functional imaging for evaluating myocardial perfusion and left ventricular function, initiated in the early 1970s, transformed coronary artery disease (CAD) management by providing valuable diagnostic and prognostic information. Over the ensuing 4 decades, improvements in imaging device sensitivity and resolution, along with dual-modality imaging (PET/CT and SPECT/CT), augmented by ultrasound (echocardiography) and MRI techniques, have provided enhanced anatomic, metabolic, and physiologic characterization of CAD and subsequent therapeutic monitoring. These tools have afforded a means to characterize CAD, typically at later stages of disease progression, guiding treatment decisions rather than informing preventive measures.

Today, another transformation looms. The availability of genomic and proteomic analysis of disease has shed light on the underlying molecular and cellular processes involved in disease initiation and progression. The ability to assess proteomic and metabolic changes early in disease, coupled with genomic information, identifying at-risk patients, gives rise to the possibility of personalized prevention and treatment strategies. One of the means by which this information may be obtained is targeted molecular imaging. Molecular imaging is a rapidly growing discipline aimed at the noninvasive visualization and characterization of cellular and molecular functions in living systems. Although targeted nuclear imaging with single-photon–radiolabeled and positron-radiolabeled probes has its roots in the pregenomic era, the process for selecting targets has changed with the abundance of new biologic information. New in vivo imaging modalities, including MRI/magnetic resonance spectroscopy, optical (fluorescence and bioluminescence) imaging, and ultrasound imaging with microbubble probes, have become available. In addition, molecular biology techniques developed to distinguish gene expression or protein–protein interactions in vitro have been translated into in vivo human imaging assays. These modalities and techniques have defined new boundaries for diagnosis and disease management.

There remains a dearth of validated probes for many diseases, including CAD. Although there is no shortage of potential molecular targets or ways to label cells for cell trafficking or imaging of gene expression (Fig. 1), identifying the right target for discriminating a particular pathway related to a specific disease is the challenge. This symposium proceeding provides an overview of the development of selected targeted molecular imaging probes for cellular and molecular assessment of cardiovascular diseases and promising therapies.

STRATEGIES AND METHODS FOR MRI LABELING OF CELLS

The clinical use of novel experimental immune and stem cell therapies requires suitable methods for monitoring cellular biodistribution noninvasively after administration. Among the different clinically used imaging techniques, MRI has superior spatial resolution, with excellent soft-tissue contrast. For exogenous therapeutic cells to be detected, they need to have contrast different from that of endogenous cells. There are several different approaches for endowing cells with MRI-visible properties (1). At present, the most sensitive and widely used MRI labels are superparamagnetic iron oxide nanoparticles (SPIOs). SPIOs are clinically approved and create strong local magnetic field disturbances that spoil the MR signal, leading to hypointense contrast. By 2009, at least 4 clinical MRI cell-tracking studies had been performed; they are reviewed in detail elsewhere (2).

Cells can be labeled with SPIOs, notably, ferumoxides injectable solution (Feridex; Bayer HealthCare Pharmaceuticals), by simple incubation (3,4) after coating with transfection agents (5) or by magnetoelectroporation (6). The optimal labeling technique depends on the cell type (i.e., whether the cell is phagocytic or difficult to transfect) and application. Paramagnetic gadolinium chelates can also be used (7), although the induced contrast can be ambiguous: positive contrast decreases at higher magnetic fields while negative,

susceptibility-based contrast increases (8). Paramagnetic gadolinium chelates have not been used clinically, and there are serious concerns about their safety for cell tracking: Free gadolinium is toxic, and this scenario may occur after prolonged retention by cells in acidic compartments (i.e., lysosomes). In addition, the issue of nephrogenic systemic fibrosis has dampened enthusiasm for initiating preliminary clinical studies (9).

Conventional approaches require cells to be prelabeled with contrast agent before injection; an alternative approach is based on in vivo labeling through cell–cell transfer (4). In that study, irradiated tumor cells, used for vaccination, were prelabeled with SPIOs and injected into the footpads of mice. Sentinel dendritic cells, which capture labeled cells followed by presentation to T cells, simultaneously phagocytose the tumor cell–associated particles. This technique has enabled MRI monitoring of in vivo antigen capture and the temporal dynamics of trafficking of dendritic cells to lymph nodes (Fig. 2) (4).

A radically different approach for cell labeling relies on chemical exchange saturation transfer contrast. Nonwater protons in chemically distinct environments, such as amide protons in peptides, exhibit a slight off-resonance frequency. Through the application of a saturation pulse, the amide protons can be wiped out of plane and rendered unable to generate a signal. Through exchange with water protons, the overall MRI signal then decreases. Various peptides with exchangeable groups can be used to label cells; furthermore, because each type of proton has its own specific off-resonance frequency, “multiple colors” can be created after image postprocessing, enabling the simultaneous detection of different cell types (10). An exciting new approach is the development of an MRI reporter gene based on this concept. A prototype amide proton–rich reporter, lysine-rich protein, has been developed and shown to be traceable in tumor cells; this strategy enables permanent prolonged cell tracking without a dilution effect, which is a problem inherent in the use of exogenous labels (11).

Another emerging application is ^{1}H MRI performed only for anatomic information in conjunction with ^{19}F as a tracer molecule. Because there is no endogenous background signal, “hot spot” images of the tracer can be obtained and superimposed on the anatomic ^{1}H images (12–14). An example is shown in Figure 3. The strategy for intracellular labeling is similar to that used for labeling with SPIOs: In this case, ^{19}F particles can be simply phagocytized (15), mixed with transfection agents (12), or electroporated into cells. At the high magnetic field strengths used in those preclinical studies (9.4 or 11.7 T), the sensitivity of MRI was approximately 140 pmol of perfluoro-polyether per cell. Such particles are stable in vivo for over 2 wk and do not affect cell viability or proliferation.

Finally, novel semipermeable microcapsules that immunoprotect cells and are visible with multiple modalities have been developed. Initially, x-ray–visible alginate capsules that contained barium or bismuth (“X caps”) were developed (16), but capsules containing SPIOs (magnetocapsules) were more recently described (17). In principal, any type of contrast agent can be coencapsulated, allowing multimodality tracking. Depending on the specific cellular imaging application, a large set of tools exists for MRI cell tracking.

PET RADIOTRACERS

Molecular imaging agents labeled with an appropriate positron emitter can be used to examine various diseases at the cellular, subcellular, or even molecular level. The use of such molecular imaging probes as radiotracers offers the opportunity to noninvasively monitor their path and fate in living subjects with PET. It is expected that PET, used as an in vivo pharmacologic imaging tool, will play an increasingly important role in earlier disease detection and improved therapeutic decision making. Cardiovascular PET will improve the understanding of molecular mechanisms relevant to cardiac disease by allowing the

visualization of specific targets and pathways that underlie changes in morphology, physiology, and function. Although several PET radiotracers have been successfully introduced into clinical trials, there is still a great demand for the development and optimization of PET radiotracers for the imaging of various targets that are relevant to cardiovascular diseases. It is anticipated that PET radiotracers will be vital elements in the emerging paradigm of personalized cardiovascular medicine.

Several positron-emitting radionuclides that can be applied to the development of successful PET radiotracers for research and clinical use are listed in Table 1. ^{11}C is an attractive and important positron-emitting isotope for labeling molecules of biologic interest, given that ^{11}C may replace ^{12}C in a molecule without changing the structure or the biologic properties. Although the half-life of ^{11}C is short (20.4 min) and multistep syntheses are generally not applicable for the radiosynthesis of ^{11}C-containing molecules, a diverse array of reactions that introduce ^{11}C into target molecules have been investigated and developed. Several nonconventional metallic isotopes with longer half-lives can be prepared at high yields in small biomedical cyclotrons, thereby expediting delivery to facilities remote from a cyclotron and allowing matching of the half-life to the lifetime of the biologic function being measured. The availability of a ^{68}Ga generator provides the opportunity to prepare PET radiotracers in facilities without a cyclotron. Isotopes with longer half-lives, such as ^{64}Cu, ^{86}Y, ^{89}Zr, and ^{124}I, are appropriate for labeling biomolecules such as peptides, proteins, antibodies, antibody fragments, and oligonucleotides. However, some of the metallic radionuclides have complex decay schemes. They usually decay with the emission of low β^+-percentage branching (^{86}Y, 33%; ^{66}Ga, 57%) and high β^+-energy (^{86}Y, 1.3 MeV; ^{66}Ga, 1.7 MeV) as well as the coemission of a substantial amount of γ-radiation; all of these properties result in increased radiation doses for patients. Therefore, it is important to consider decay pathways and other properties, such as half-life and positron energy, before selecting the appropriate isotope for labeling the desired tracer.

PET Radiotracers with ^{18}F

^{18}F appears to be an ideal radionuclide for routine PET because of its almost perfect chemical and nuclear properties. Compared with other short-lived radionuclides, such as ^{11}C, ^{18}F has a half-life of 109.8 min, which is long enough to allow time-consuming multistep radiosyntheses as well as imaging procedures extended over several hours. In addition, the low β^+-energy of ^{18}F, 0.64 MeV, promises a short positron linear range in tissue, contributing to high-resolution PET images.

Depending on the production method, ^{18}F is obtained in a particular chemical form, either ^{18}F-gas (^{18}F-F_2) or ^{18}F-fluoride ion (^{18}F-F^-), which determines the possible reactions. The principal ^{18}F labeling strategies are restricted to a few and can be divided into approximately 2 distinct groups: direct fluorination, in which the ^{18}F radionuclide is introduced “directly” into the target molecule in a single step, and indirect fluorination, in which a prosthetic group is used and multistep synthesis is usually required. Prosthetic groups typically bear reactive functional groups that are readily conjugated to biomolecules. Direct fluorination strategies can be further subdivided into 2 major areas of fluorination: electrophilic and nucleophilic. Of these 2 methods, electrophilic ^{18}F fluorination methods, with reagent ^{18}F-F_2 gas, are less favorable because of limited availability, nonspecific labeling, and low specific activity of the labeled products.

Because ^{18}F-FDG was evaluated for the first time in 1978 (18), it has become the most important radiopharmaceutical in clinical PET. ^{18}F-FDG is predominantly used not only for tumor imaging but also for myocardial viability assessment (19–21). More recently, ^{18}F-FDG was successfully used for the imaging of atherosclerotic plaque inflammation (22) and the labeling of stem cells for tracking after transplantation (23).

Direct labeling with nucleophilic ^{18}F-F$^-$ generally requires reaction conditions, such as a high temperature and a strong base, that may not be appropriate for the labeling of biomolecules. To facilitate biomolecule labeling, researchers have developed ^{18}F-containing prosthetic groups (Fig. 4) for labeling under mild reaction conditions; these have been used for ^{18}F fluoroalkylation, ^{18}F fluoroacylation, and ^{18}F fluoroamidation of primary amino groups at the N terminus or lysine residues and thiols on cysteine residues. An ^{18}F-labeled glycosylated $\alpha_v\beta_3$-integrin antagonist (^{18}F-galacto-RGD), prepared through ^{18}F-fluoropropionic acid conjugation, specifically targets $\alpha_v\beta_3$-integrin expression (24–26). Successful monitoring of $\alpha_v\beta_3$-integrin expression in tumors has already been reported in animal and human clinical studies. A recent study demonstrated for the first time the feasibility of measuring myocardial integrin expression in vivo noninvasively with ^{18}F-galacto-RGD PET (27). Focal ^{18}F-galacto-RGD uptake was observed after a brief episode of coronary occlusion and reperfusion (Fig. 5). In addition, successful synthesis of ^{18}F-annexin V with ^{18}F-succinimidyl fluorobenzoate as a prosthetic group for apoptosis imaging has been reported (28). In ischemic animals, the accumulation of ^{18}F-annexin V in the infarcted area was about 3-fold higher than that in the noninfarcted area. Apoptosis was widely detected only in the infarcted area of the left ventricle with hematoxylin–eosin stain. The accumulation of ^{18}Fannexin V in the left ventricular infarcted area 24 h after ischemia matched the infarcted area detected with 2,3,5-triphenyltetrazolium chloride stain (Fig. 6).

PET Radiotracers with ^{11}C

Almost all ^{11}C-labeled PET tracers are made from 2 major cyclotron-produced precursors, ^{11}C-carbon dioxide ($^{11}CO_2$) and ^{11}C-methane ($^{11}CH_4$). ^{11}C-methyl iodide (^{11}C-CH_3I), the most versatile methylation agent, is prepared through reduction and iodination of ^{11}C-CO_2. ^{11}C-methyl triflate (^{11}C-CH_3OTf), produced from ^{11}C-CH_3I, has also been used for methylation. Facile methylation of amines, thiols, and alcohols involves simple trapping of ^{11}C-CH_3I or ^{11}C-CH_3OTf in a solution of the target precursor and subsequent heating or interaction with a precursor coating the interior of a loop of small tubing.

Several ^{11}C radiotracers (Fig. 7) used for cardiac PET have been synthesized through ^{11}C methylation: ^{11}C-meta-hydroxyephedrine, ^{11}C-epinephrine, and ^{11}C-phenylephrine for the imaging of sympathetic neuronal catecholamine uptake, storage, and turnover (29–31); 17-^{11}C-heptadecanoic acid and ^{11}C-palmitic acid for the imaging of fatty acid metabolism (32–35); ^{11}C-acetate to probe oxidative metabolism through the tricarboxylic acid cycle (36,37); and ^{11}C-GB67 for imaging of the α_1-adrenergic receptor (38). Recent developments in ^{11}C radiochemistry are further stimulating the progress of PET as a powerful imaging technique in research and clinical use.

PET Radiotracers with Nonconventional Radionuclides

^{64}Cu can be effectively produced by both reactor-based and accelerator-based methods. During the last decade, there has been considerable research interest in the development of ^{64}Cu-labeled PET tracers for targeting specific receptors or antigens. ^{64}Cu is conjugated to these targeting ligands by a chelator that is attached through a functional group. A comprehensive review (39) summarized the potential application of various chelating agents to the production of ^{64}Cu-labeled PET tracers. Recently, a study of vascular endothelial growth factor (VEGF) receptor expression kinetics in a rat myocardial infarction (MI) model was undertaken with ^{64}Cu-DOTA-$VEGF_{121}$ as the PET tracer (40). VEGF is the most prominent member of a family of growth factors that have been strongly associated with angiogenic stimuli in various pathophysiologic situations and likely plays a role in left ventricular remodeling after MI. ^{64}Cu-DOTA-$VEGF_{121}$ PET scans were performed before MI induction (produced by ligation of the left anterior descending coronary artery and confirmed by ultrasound) and at days 3, 10, 17, and 24 after MI induction. The results (Fig.

8) showed that ^{64}Cu-DOTA-VEGF$_{121}$ myocardial uptake after MI was significantly higher (up to 1.0 ± 0.1 percentage injected dose per gram [%ID/g]) than the baseline myocardial uptake (0.3 ± 0.1 %ID/g).

The use of a generator is a less expensive and convenient alternative to an on-site cyclotron for the production of short-lived radionuclides. ^{68}Ga decays by 89% through positron emission of 1.92 MeV (maximum energy), and it can be produced from an in-house generator system consisting of an inorganic or organic matrix immobilizing the parent radionuclide, ^{68}Ge (half-life, 270.8 d). The well-established coordination chemistry of Ga^{3+} facilitates the development of a ^{68}Ga-containing PET tracer. The Ga^{3+} ion is classified as a hard Lewis acid, which is able to form thermodynamically stable complexes with ligands that are hard Lewis bases. Ligands with carboxylate, phosphonate, amino groups, and thiol groups are usually good chelating agents for Ga^{3+}. A direct PET application of a ^{68}Gacontaining tracer, ^{68}Ga-[bis(4,6-dimethoxysalicylaldimino)-*N*,*N*′-bis(3-aminopropyl)ethylenediamine]$^{+}$, was reported; after intravenous injection, this tracer exhibited significant myocardial uptake and then prolonged myocardial retention (41). In addition, 3 cyclic arginine–glycine–aspartic acid (RGD) peptides, c(RGDyK) (RGD1), E[c(RGDyK)]$_2$ (RGD2), and E{E[c(RGDyK)]$_2$}$_2$ (RGD4), were conjugated with a macrocyclic chelator (1,4,7-triazacyclononane-1,4,7-triacetic acid [NOTA]), labeled with ^{68}Ga, and evaluated for the imaging of $\alpha_v\beta_3$-integrin expression in vivo (42). All 3 ^{68}Ga-NOTA–conjugated peptides showed a good affinity for $\alpha_v\beta_3$-integrin in a cell-based binding assay. The dimeric RGD peptide tracer ^{68}Ga-NOTA-RGD2 had the most favorable pharmacokinetics, with good tumor uptake and retention, warranting further investigation for potential clinical translation to the imaging of $\alpha_v\beta_3$-integrin (Fig. 9).

BISPECIFIC ANTIBODIES AND POLYLINKAGE METHODS FOR SPECT

In vivo imaging with radiolabeled antibodies has been somewhat successful in oncology and cardiovascular diseases. The success is due to the availability of sufficient concentrations of the targeted antigens. For the imaging of MI, there are ample targets for radiolabeled antibody localization to enable visualization after a waiting period of hours. The ample number of targets is due to the exposure of large amounts of the antigen, in this case, cardiac myosin, to the extracellular milieu after cell membrane disruption because contiguous masses of myocardium are affected in acute MI. However, coronary atherosclerotic lesions are much smaller than acute MI. Atherosclerotic lesions are smaller than the diameter of coronary vessels; therefore, the concentration of a potential target is minimal. In vivo imaging of minimal target lesions may be enabled by substantially increasing the specific activity of the targeting reagent while minimizing the nontarget background activity. A marriage of bispecific antibody pretargeting technology (43) and nanopolymer signal amplification technology has been used to achieve suitable in vivo imaging (44). The former provides specificity for targeting, and the latter provides the potential to develop targeted probes with high specific radioactivity. Such an approach may also be applicable for the imaging of small metastatic lesions (45) and may enable the targeted delivery of therapeutic drug formulations with high specific activity. The feasibility of this concept of targeting with high-specific-activity probes pretargeted with bispecific antibodies has been demonstrated in a model system, ApoE-deficient (ApoE-knockout) mice with experimental atherosclerotic lesions (44). Similar imaging probes may well be applicable in cancer imaging and therapy.

In acute MI, 1 g of myocardium provides about 60 mg of myosin (about 1.2×10^{-7} mol) (45). This amount translates to the availability of 7.2×10^{16} molecules of myosin. Even if only 1% of the available myosin were bound by antibodies, then 7.2×10^{14} molecules of antimyosin would be bound to myosin. In a clinical study (46), 0.5 mg (10^{-8} mol) of

antimyosin Fab was labeled with either about 740–925 MBq of ^{99m}Tc (44) or 74 MBq of ^{111}In (47). The specific radioactivity of the ^{99m}Tc-labeled antimyosin Fab was approximately 1:5 (^{99m}Tc to antibody). The specific activity of the antimyosin antibody was much higher than that of other radiopharmaceuticals, such as ^{99m}Tc-glucoheptonate ($1:1.2 \times 10^6$) or ^{99m}Tc-glucarate ($1:1 \times 10^5$). Therefore, if a probe with a minimum molar ratio of 1:1 (^{99m}Tc to probe) can be obtained, then high-specific-activity probes will be available for in vivo targeting.

A biodistribution study of ^{99m}Tc-labeled diethylenetria-minepentaacetic acid (DTPA)–conjugated succinylated polylysine (15,000 kDa) in normal Sprague–Dawley rats showed that at 24 h after intravenous injection, the only organs with significant radioactivity were the kidneys (0.345 ± 0.054 %ID/g). Other activities were near the baseline. However, when this ^{99m}Tc-labeled polymer was injected after pretargeting of the model antigen–coated beads in vivo with a bispecific antibody, samples of 4 μg of surrogate antigen beads in 100 μL of phosphate-buffered saline were detectable and visualized in rats. Because the antigen was injected intramuscularly, the imaging was not equivalent to the imaging of intravascular atherosclerotic lesions. However, this model might be similar to extravascular tumor models.

An ApoE knockout mouse that was on a hyperlipidemic diet and that had femoral endothelial denudation was developed to demonstrate that small atherosclerotic lesions can be detected by in vivo γ-imaging (44). In this model, femoral atherosclerotic lesions as small as 1–5 mg were visualized in all mice with experimental lesions by 3 h after intravenous administration of the ^{99m}Tc-polymer (Fig. 10). The in vivo target-to-nontarget activity ratio determined from the images was 12:1. At 2–3 h after intravenous injection of the ^{99m}Tc-polymer, there was still residual blood activity (2–3 %ID/g). Nevertheless, very small lesions were visualized because of the high specific activity of the probe.

Because of the potential for the targeted delivery of high specific activity probes to image small atherosclerotic lesions, it may also be possible to image very small tumors by pretargeting with anticancer bispecific antibodies and then targeting with either radiotracers (48) or therapeutic drug–loaded polymers (49). Furthermore, loading of toxic chemotherapeutic drugs on various polymers has resulted in decreased nontarget toxicity and increased tumor toxicity (50) because of the targeting of large tumors through the enhanced permeability retention phenomenon (51). It has been proposed that if metastatic lesions can be detected when they are still very small, then targeted therapy can also be more efficient at this stage. Combining the less toxic prodrug-loaded polymers with bispecific antibody complex pretargeting should enable the in vivo imaging of very small lesions and provide the targeted delivery of prodrug-loaded polymers for highly efficient targeted cancer therapy. Preliminary in vitro cancer cell culture (49) and in vivo imaging (48) studies showed that prodrug-loaded polymers were less toxic to nontumor cells and that after pretargeting with bispecific antibody complexes, tumor toxicity increased to 150% of that obtained with free chemotherapeutic drug treatment. The visualization of tumor masses with diameters of less than 1 mm was also achieved when technetium (48) or ^{111}In radioactive isotopes were substituted for the chemotherapeutic drugs on the polymers.

Thus, signal amplification with polymers for the targeted delivery of either radiotracers or prodrugs may result in the ability to image very small lesions in the cardiovascular or oncology arena. It may also lead to the ability to deliver high concentrations of therapeutic drugs in the prodrug form to achieve highly specific targeted chemotherapy of cancer or adequate delivery of therapeutic agents to the myocardium.

TARGETED NANOPARTICLES

There are great expectations for multifunctional nanoparticles (Fig. 11) to provide noninvasive detection, diagnosis, treatment, and monitoring of disease progression, regression, and recurrence. However, there remain great challenges for applying them while achieving selective tissue targeting in vivo at increasing levels of imaging sensitivity. Nanoscopic materials occupy a critical position between the macroscopic world and the molecular level and can be designed to offer unique advantages over both macroscopic materials and molecular systems. It is no wonder that biology builds complexity into systems in a hierarchical fashion. Ions, small molecules, and macromolecules are combined through supramolecular interactions and covalent linkages into functional systems (e.g., proteins, enzymes, genes, lipoproteins, and viruses); these systems have dimensions of 5–100 nm, can perform sophisticated functions, and were recently labeled “nanomachines.” As structures are built from their constituent parts, the ratio of the surface area to the volume decreases. For instance, for a spheric object, the surface area increases by a factor of r^2, whereas the volume increases cubically; the surface area– to–volume ratio, therefore, decreases with increasing sphere radius. Considered in the opposite sense, the volume–to–surface area ratio increases with increasing diameter, so that during building from small molecules or macromolecules to nanoscale structures, an internal volume is created. This characteristic has generated significant interest in synthetic nanomaterials that can serve as vessels for the transport and delivery of imaging and therapeutic agents. Nanoscopic objects possess internal packaging capacity, as is possible for larger structures but not for small molecules, and a sufficient surface area for the presentation of multiple types and numbers of active elements; that is, they can be designed to have an optimal balance of internal volume and external surface area.

Analogies have often been drawn between synthetic nanomaterials and biologic nanomachines, and those biologic systems provide inspiration and design elements for functional biologic mimics and routes toward their manufacture. Well-defined chemistries are allowing for distinct control over the surface, shell, and core compositions and properties throughout the nanoscopic frameworks. Overall, the physical characteristics (e.g., size and shape) lead to unique in vivo trafficking, with further manipulation of tissue-selective targeting being facilitated most commonly through molecular recognition events borrowed from nature. Biologically active ligands are often conjugated to nanostructures so that they are accessible to the surface and available for binding with biologic receptors, resulting in synthetic–biologic hybrid materials. The large internal capacity of nanoscale structures can then be used for the packaging of molecular imaging elements or pharmaceutical agents. These features have led to an emerging field of nanomedicine and to the development of new diagnostic and pharmacodiagnostic agents.

The promising attributes of nanomaterials for targeted imaging include their ability to deliver large numbers of imaging agents per targeted molecular recognition event to achieve high-sensitivity imaging and their ability to deliver several different types of imaging agents to perform multimodality imaging (Fig. 12). In comparison with small-molecule systems, which are capable of detecting molecular recognition events to identify disease or injury through the use of one label for each targeting moiety, the conjugation of a targeting ligand to a nanoscale platform carrying large quantities of labels is designed to enhance the sensitivity of detection.

There are many types of nanoparticle platforms, with different compositions (organic vs. inorganic), structures, shapes, and sizes that can be used to carry labels for different kinds of imaging. Many different biologic tissues or disease sites can be targeted, creating a substantial research and development space. Nanoparticle structures being evaluated for

biomedical applications include dendrimers (52), polymeric micelles (53), liposomes (54), nonviral nanoparticles (55), lipoprotein nanoparticles (56), metallic nanoparticles (57), and carbon nanotubes (58). Moreover, there are many synthesis strategies by which any particular labeled nanoparticle can be prepared for imaging applications; these can involve various combinations and stages of nanoparticle production and introduction of labels, targeting ligands, and other components. As building blocks are combined to establish nanoscopic materials, it becomes increasingly challenging to determine composition and structure accurately. Therefore, it is important to balance which functionalities are incorporated at which stage: Some units, especially those that have a detectable signature, can be attached after the nanoparticle is produced (postnanoparticle functionalization), whereas others should be accounted for at earlier stages (prefunctionalization of nanoparticle precursor components). For any nanoparticle material, rigorous physicochemical characterization studies are essential to determine accurately the structure and properties of the material, including the surface and subsurface chemistries and morphologies.

Organic polymer–derived nanoparticles are a promising nanoparticle platform because of versatility in structure, composition, size, morphology, and flexibility; diverse, orthogonal chemical reactions for the incorporation of multiple numbers and types of functionalities; and potential for biodegradability. Even inorganic nanoparticles are often coated with polyethylene glycol (PEG), an organic polymer, to inhibit protein adsorption and thereby avoid rapid clearance by the mononuclear phagocytic system in vivo. Because the degree of PEG coverage of nanoparticle surfaces can lead to dramatic changes in protein adsorption (59,60), quantification of the extent of pegylation is important. However, PEG has no chromophore, and its attachment to a preestablished nanoparticle makes the determination of PEG coverage challenging. In contrast, its conjugation to the backbone of a polymer precursor, followed by the assembly of nanostructures, has allowed for accurate variability in pegylation, which has been shown to produce significant differences in blood circulation times versus elimination in clearance organs for shell cross-linked knedel-like nanoparticles with diameters of approximately 15–20 nm (Fig. 13) (61). Moreover, prefunctionalization of polymer precursors with chelators for radiolabels has provided enhancements in labeling. For instance, the conjugation of macrocyclic DOTA units at the polymer stage (Fig. 13) produced hundreds of ^{64}Cu labels per nanoparticle, whereas the conjugation of macrocyclic DOTA units to a preestablished nanoparticle experienced limitations (62). Of course, there are methods for accomplishing highly efficient radiolabeling of preestablished nanoparticles. In an interesting recent example, “click chemistry” was used to attach large numbers of fluorine atoms (63). It has been reported that, with this approach, doses of nanoparticles 2–4 orders of magnitude lower than those required for MRI can be used.

Advances toward the development of multimodality agents, for which a single nanoparticle can be used for combinations of PET, MRI, optical imaging, or other modalities, have been described (57). For instance, PET and optical probes were attached to inorganic particles for both CT and MRI. In another example, targeting ligands were attached to a magnetic nanoparticle platform, allowing both PET and MRI (64). The ability to administer a small mass of particles likely will allow the more rapid translation of agents to clinics.

As nanotechnology continues to be developed for medical applications, including in vivo imaging, 2 primary challenges that require significant attention are improving tissue-selective targeting and providing mechanisms for the ultimate clearance of the materials once their task is complete. Each of these will be addressed through collaborative efforts by chemists who can design and construct the nanomaterials with exquisite control over all aspects of the structures and properties; physical scientists who can probe the compositions, structures, and properties with high degrees of accuracy throughout the nanoscale frameworks; biologists who can investigate the interactions between the synthetic materials

and their biologic targets; and clinicians who can define the directions the materials should take while evaluating their performance in reaching, detecting, and affecting their intended targets.

IMAGING OF ISCHEMIC TISSUE WITH INTEGRIN-TARGETED NANOPARTICLES

Advances in nanoparticle design and synthesis have led to the development of targeted delivery of agents. Specific targeting mechanisms, such as target moiety conjugation to the carrier, allow for selective direction and increased drug accumulation at target sites and thereby lead to greater diagnostic or therapeutic efficacy. Receptor targeting strategies are particularly valuable because a variety of cell surface receptors are upregulated in cancerous cells and other disease states, providing clear markers for drug delivery or imaging systems. One of the targets widely studied for imaging and drug delivery systems is $\alpha_v\beta_3$-integrin, a well-known cell surface disease biomarker that is upregulated in the angiogenic vessels associated with diseases such as cancer, cardiomyopathy, atherosclerosis, and peripheral arterial disease (65). In the cardiovascular setting, angiogenesis is triggered by hypoxia and ischemia, and its major consequence in tissues is the restoration of perfusion and oxygenation. Proangiogenic therapies are aimed at stimulating the growth of new blood vessels to improve tissue function. Consequently, there has been active clinical interest in the evaluation of angiogenic factors such as $\alpha_v\beta_3$-integrin.

As part of a multidisciplinary collaboration among scientists and physicians from several academic institutions, nanoparticle constructs targeting $\alpha_v\beta_3$-integrin are being evaluated as biomarkers for cardiovascular diseases. In vitro isolated integrin-binding assays have been optimized to compare the heterologous competitive binding of biotinylated vitronectin and RGD (targeting) peptide–nanoparticle constructs to $\alpha_v\beta_3$-integrin as well as to determine the specificity of monomeric peptides and peptide–nanoparticle conjugates for $\alpha_v\beta_3$-integrin, $\alpha_v\beta_5$-integrin, and $\alpha_{IIb}\beta_3$-integrin. Because binding affinity alone does not predict whether an agent will succeed as an in vivo imaging agent, compounds with higher affinities are evaluated for their internalization in $\alpha_v\beta_3$-integrin–positive tumor cell lines before in vivo imaging. Thus far, over 70 different peptides and peptide–nanoparticle constructs have been evaluated in heterologous binding assays with $\alpha_v\beta_3$-integrin, and a majority of these have been assayed for their specificity for $\alpha_v\beta_5$-integrin or $\alpha_{IIb}\beta_3$-integrin. Of these agents, about 15 have been investigated for cell-associated activity in U87 glioblastoma or M21/M21L melanoma cells. Approximately 10 compounds have been investigated in a mouse model of hind limb ischemia (52).

At present, the agent with the most optimal specific uptake in the hind limb ischemia model is an RGD dendrimer that has been labeled with the positron emitter ^{76}Br (half-life, 17 h) and the γ-emitter ^{125}I (half-life, 60 d) (52). The RGD dendrimer nanoprobe was designed to be biodegradable, with a modular multivalent core–shell architecture consisting of a biodegradable heterobifunctional dendritic core chemoselectively functionalized with heterobifunctional polyethylene oxide (PEO) chains that formed a protective shell. The PEO chains imparted biologic stealth and dictated the pharmacokinetics (Fig. 14). Each of the 8 branches of the dendritic core was functionalized for labeling with radiohalogens. The placement of radioactive moieties at the core was designed to prevent in vivo dehalogenation, a potential problem for imaging and therapy. Targeting peptides of cyclic RGD motifs were installed at the terminal ends of the PEO chains to enhance their accessibiliy to $\alpha_v\beta_3$-integrin receptors. This nanoscale design enabled a 50-fold enhancement of the binding affinity to $\alpha_v\beta_3$-integrin receptors with respect to the monovalent RGD peptide alone, from 10.40 nM to 0.18 nM IC_{50}. Cell-based assays of the ^{125}I-labeled dendritic nanoprobe with $\alpha_v\beta_3$-integrin–positive cells revealed a 6-fold

increase in $\alpha_v\beta_3$-integrin receptor–mediated endocytosis of the targeted nanoprobe over that of the nontargeted nanoprobe, whereas $\alpha_v\beta_3$-integrin–negative cells showed no enhancement of cell uptake over time (Fig. 15). In vivo biodistribution studies of the ^{76}Br-labeled dendritic nanoprobe revealed excellent bioavailability for the targeted and nontargeted nanoprobes. In vivo studies with a murine hind limb ischemia model for angiogenesis revealed a high level of specific accumulation of the ^{76}Br-labeled dendritic nanoprobe targeted to $\alpha_v\beta_3$-integrin in angiogenic muscles, allowing highly selective imaging of this critically important process (Fig. 16).

More recently, the hypothesis of improved cell binding, internalization, and selectivity of multivalent nanoparticles over their monovalent counterparts was tested against $\alpha_v\beta_3$-integrin using comb nanoparticles with various RGD loadings. Nontargeted comb nanoparticles were initially designed and optimized for achieving an ideal pharmacokinetic imaging profile (66). The basic comb structures represent a new class of core–shell nanoparticles synthesized through the controlled collapse of well-defined comb copolymers containing a hydrophobic polymethyl methacrylate backbone, water-soluble PEG chains, and active ester groups that allow the attachment of functional moieties. For the evaluation of targeting, the optimized comb structure was functionalized with $\alpha_v\beta_3$-integrin–targeting groups and a DOTA chelator for radiolabeling with ^{64}Cu. Synthetic flexibility led to the tunable production of nanoparticle constructs with 4 different RGD loadings, referred to here as 5%, 10%, 20%, and 50%targeted nanoparticles with 7, 14, 28, and 70 RGD peptides per comb nanoparticle, respectively.

One of the important goals of the study was to understand the effects of the structure–activity relationship and multivalency on integrin binding, specificity, and cellular internalization at molecular levels. Surface proteins and receptors are relatively easier targets for such systems because the targeting ligand does not have to gain access to the inside of the diseased cell. The isolated integrin assay results demonstrated improved binding affinity for $\alpha_v\beta_3$-integrin resulting from the increase in RGD units on the nanoparticles, with 50% RGD nanoparticles having 78- fold-higher affinity (1.1 nM) than their 5% RGD counterparts (78 nM). There was no significant binding (>1,000 nM) to $\alpha_v\beta_5$-integrin (found on macrophages) or $\alpha_{IIb}\beta_3$-integrin (found on blood platelets). Cell-based assays of the ^{64}Cu-labeled nanoparticles revealed receptor-mediated endocytosis in U87MG cells, with up to 35% cellular uptake per milligram of protein at 30 min after injection. Confocal microscopy of U87MG cells incubated with targeted nanoparticles further validated cellular internalization. Currently, this class of agents is being investigated in the hind limb ischemia and U87MG tumor mouse models.

CONCLUSION

The potential of molecular imaging to aid in early diagnosis and development of curative and preventive therapies for cardiovascular diseases relies on the successful development of imaging probes and the continued evolution of imaging hardware. This review focused on the development of an array of probes already being evaluated or with promise for future applications in cardiovascular disease imaging. A variety of strategies have been identified for tagging cells to monitor stem cell therapy, imaging gene expression to monitor gene therapy, labeling small-molecules and biomolecule probes with sensitive positron-emitting isotopes, using bispecific antibodies to increase probe sensitivity and specificity, and developing nanomolecular platforms for imaging and therapy. Successful application of these imaging probes will increase the understanding of disease processes and identify ways to improve therapeutic interventions.

It takes a multidisciplinary team of scientists, including chemical biologists and molecular biologists to identify appropriate targets and develop tests to assess probe specificity, chemists from multiple disciplines to synthesize targeting molecular platforms and conjugate imaging reporters, physicists to develop imaging hardware and reconstruction algorithms, medical physicists to assist with probe validation, and physician scientists to translate probes into clinical use. Just as imaging transformed the diagnosis and treatment of CAD nearly 4 decades ago, the field is again at a transformative precipice that will further enable the management of a variety of cardiovascular diseases through the characterization of molecular signatures.

REFERENCES

1. Long CM, Bulte JW. In vivo tracking of cellular therapeutics using magnetic resonance imaging. Expert Opin Biol Ther. 2009; 9:293–306. [PubMed: 19216619]
2. Bulte JW. In vivo MRI cell tracking: clinical studies. AJR. 2009; 193:314–325. [PubMed: 19620426]
3. de Vries IJ, Lesterhuis WJ, Barentsz JO, et al. Magnetic resonance tracking of dendritic cells in melanoma patients for monitoring of cellular therapy. Nat Biotechnol. 2005; 23:1407–1413. [PubMed: 16258544]
4. Long CM, van Laarhoven HW, Bulte JW, Levitsky HI. Magnetovaccination as a novel method to assess and quantify dendritic cell tumor antigen capture and delivery to lymph nodes. Cancer Res. 2009; 69:3180–3187. [PubMed: 19276358]
5. Frank JA, Miller BR, Arbab AS, et al. Clinically applicable labeling of mammalian and stem cells by combining superparamagnetic iron oxides and transfection agents. Radiology. 2003; 228:480–487. [PubMed: 12819345]
6. Walczak P, Kedziorek DA, Gilad AA, Lin S, Bulte JW. Instant MR labeling of stem cells using magnetoelectroporation. Magn Reson Med. 2005; 54:769–774. [PubMed: 16161115]
7. Anderson SA, Lee KK, Frank JA. Gadolinium-fullerenol as a paramagnetic contrast agent for cellular imaging. Invest Radiol. 2006; 41:332–338. [PubMed: 16481917]
8. Trattnig S, Pinker K, Ba-Ssalamah A, Nöbauer-Huhmann IM. The optimal use of contrast agents at high field MRI. Eur Radiol. 2006; 16:1280–1287. [PubMed: 16508769]
9. Thomsen HS, Marckmann P, Logager VB. Update on nephrogenic systemic fibrosis. Magn Reson Imaging Clin N Am. 2008; 16:551–560. [PubMed: 18926421]
10. McMahon MT, Gilad AA, DeLiso MA, Berman SM, Bulte JW, van Zijl PC. New “multicolor” polypeptide diamagnetic chemical exchange saturation transfer (DIACEST) contrast agents for MRI. Magn Reson Med. 2008; 60:803–812. [PubMed: 18816830]
11. Gilad AA, McMahon MT, Walczak P, et al. Artificial reporter gene providing MRI contrast based on proton exchange. Nat Biotechnol. 2007; 25:217–219. [PubMed: 17259977]
12. Ahrens ET, Flores R, Xu H, Morel PA. In vivo imaging platform for tracking immunotherapeutic cells. Nat Biotechnol. 2005; 23:983–987. [PubMed: 16041364]
13. Bulte JW. Hot spot MRI emerges from the background. Nat Biotechnol. 2005; 23:945–946. [PubMed: 16082363]
14. Partlow KC, Chen J, Brant JA, et al. ^{19}F magnetic resonance imaging for stem/ progenitor cell tracking with multiple unique perfluorocarbon nanobeacons. FASEB J. 2007; 21:1647–1654. [PubMed: 17284484]
15. Ruiz-Cabello J, Walczak P, Kedziorek DA, et al. In vivo “hot spot” MR imaging of neural stem cells using fluorinated nanoparticles. Magn Reson Med. 2008; 60:1506–1511. [PubMed: 19025893]
16. Barnett BP, Kraitchman DL, Lauzon C, et al. Radiopaque alginate microcapsules for X-ray visualization and immunoprotection of cellular therapeutics. Mol Pharm. 2006; 3:531–538. [PubMed: 17009852]
17. Barnett BP, Arepally A, Karmarkar PV, et al. Magnetic resonance-guided, realtime targeted delivery and imaging of magnetocapsules immunoprotecting pancreatic islet cells. Nat Med. 2007; 13:986–991. [PubMed: 17660829]

18. Gallagher BM, Fowler JS, Gutterson NI, MacGregor RR, Wan CN, Wolf AP. Metabolic trapping as a principle of oradiopharmaceutical design: some factors responsible for the biodistribution of ^{18}F-2-deoxy-2-fluoro-D-glucose. J Nucl Med. 1978; 19:1154–1161. [PubMed: 214528]
19. Ghesani M, Depuey EG, Rozanski A. Role of F-18 FDG positron emission tomography (PET) in the assessment of myocardial viability. Echocardiography. 2005; 22:165–177. [PubMed: 15693785]
20. Segall G. Assessment of myocardial viability by positron emission tomography. Nucl Med Commun. 2002; 23:323–330. [PubMed: 11930185]
21. Slart RH, Bax JJ, van Veldhuisen DJ, van der Wall EE, Dierckx RA, Jager PL. Imaging techniques in nuclear cardiology for the assessment of myocardial viability. Int J Cardiovasc Imaging. 2006; 22:63–80. [PubMed: 16372139]
22. Bengel FM. Atherosclerosis imaging on the molecular level. J Nucl Cardiol. 2006; 13:111–118. [PubMed: 16464725]
23. Beeres SL, Bengel FM, Bartunek J, et al. Role of imaging in cardiac stem cell therapy. J Am Coll Cardiol. 2007; 49:1137–1148. [PubMed: 17367656]
24. Haubner R, Kuhnast B, Mang C, et al. [^{18}F]galacto-RGD: synthesis, radiolabeling, metabolic stability, and radiation dose estimates. Bioconjug Chem. 2004; 15:61–69. [PubMed: 14733584]
25. Haubner R, Weber WA, Beer AJ, et al. Noninvasive visualization of the activated alphavbeta3 integrin in cancer patients by positron emission tomography and [^{18}F]galacto-RGD. PLoS Med. 2005; 2:e70. [PubMed: 15783258]
26. Haubner R, Wester HJ. Radiolabeled tracers for imaging of tumor angiogenesis and evaluation of anti-angiogenic therapies. Curr Pharm Des. 2004; 10:1439–1455. [PubMed: 15134568]
27. Higuchi T, Bengel FM, Seidl S, et al. Assessment of alphavbeta3 integrin expression after myocardial infarction by positron emission tomography. Cardiovasc Res. 2008; 78:395–403. [PubMed: 18256073]
28. Murakami Y, Takamatsu H, Taki J, et al. ^{18}F-labelled annexin V: a PET tracer for apoptosis imaging. Eur J Nucl Med Mol Imaging. 2004; 31:469–474. [PubMed: 14666384]
29. Del Rosario RB, Jung YW, Caraher J, Chakraborty PK, Wieland DM. Synthesis and preliminary evaluation of [^{11}C]-(−)-phenylephrine as a functional heart neuronal PET agent. Nucl Med Biol. 1996; 23:611–616. [PubMed: 8905825]
30. Munch G, Nguyen NT, Nekolla S, et al. Evaluation of sympathetic nerve terminals with [^{11}C]epinephrine and [^{11}C]hydroxyephedrine and positron emission tomography. Circulation. 2000; 101:516–523. [PubMed: 10662749]
31. Vesalainen RK, Pietila M, Tahvanainen KU, et al. Cardiac positron emission tomography imaging with [^{11}C]hydroxyephedrine, a specific tracer for sympathetic nerve endings, and its functional correlates in congestive heart failure. Am J Cardiol. 1999; 84:568–574. [PubMed: 10482157]
32. Collier TL, Hwang Y, Ramasamy R, et al. Synthesis and initial evaluation of 17-^{11}C-heptadecanoic acid for measurement of myocardial fatty acid metabolism. J Nucl Med. 2002; 43:1707–1714. [PubMed: 12468523]
33. Schelbert HR, Benson L, Schwaiger M, Perloff J. Positron emission tomography: the technique and its applications to the study of the cardiovascular system. Cardiol Clin. 1983; 1:501–520. [PubMed: 6336182]
34. Schelbert HR, Henze E, Keen R, et al. C-11 palmitate for the noninvasive evaluation of regional myocardial fatty acid metabolism with positron-computed tomography. IV. In vivo evaluation of acute demand-induced ischemia in dogs. Am Heart J. 1983; 106:736–750. [PubMed: 6604447]
35. Schön HR, Schelbert HR, Najafi A, et al. C-11 labeled palmitic acid for the noninvasive evaluation of regional myocardial fatty acid metabolism with positron-computed tomography. II. Kinetics of C-11 palmitic acid in acutely ischemic myocardium. Am Heart J. 1982; 103:548–561. [PubMed: 6801945]
36. Buck A, Wolpers HG, Hutchins GD, et al. Effect of carbon-11-acetate recirculation on estimates of myocardial oxygen consumption by PET. J Nucl Med. 1991; 32:1950–1957. [PubMed: 1919738]
37. Buxton DB, Schwaiger M, Nguyen A, Phelps ME, Schelbert HR. Radiolabeled acetate as a tracer of myocardial tricarboxylic acid cycle flux. Circ Res. 1988; 63:628–634. [PubMed: 3136951]

38. Law MP, Osman S, Pike VW, et al. Evaluation of [^{11}C]GB67, a novel radioligand for imaging myocardial alpha 1-adrenoceptors with positron emission tomography. Eur J Nucl Med. 2000; 27:7–17. [PubMed: 10654141]
39. Sun X, Anderson CJ. Production and applications of copper-64 radiopharmaceuticals. Methods Enzymol. 2004; 386:237–261. [PubMed: 15120255]
40. Rodriguez-Porcel M, Cai W, Gheysens O, et al. Imaging of VEGF receptor in a rat myocardial infarction model using PET. J Nucl Med. 2008; 49:667–673. [PubMed: 18375924]
41. Tsang BW, Mathias CJ, Green MA. A gallium-68 radiopharmaceutical that is retained in myocardium:^{68}Ga[(4,6-MeO_2sal)$_2$BAPEN]$^+$ J Nucl Med. 1993; 34:1127–1131. [PubMed: 8315489]
42. Li ZB, Chen K, Chen X. ^{68}Ga-labeled multimeric RGD peptides for microPET imaging of integrin alpha(v)beta(3) expression. Eur J Nucl Med Mol Imaging. 2008; 35:1100–1108. [PubMed: 18204838]
43. Brennan M, Davison PF, Paulus H. Preparation of bispecific antibodies by chemical recombination of monoclonal immunoglobulin G1 fragments. Science. 1985; 229:81–83. [PubMed: 3925553]
44. Khaw BA, Tekabe Y, Johnson LL. Imaging experimental atherosclerotic lesions in ApoE knockout mice: enhanced targeting with Z2D3-anti-DTPA bispecific antibody and^{99m}Tc-labeled negatively charged polymers. J Nucl Med. 2006; 47:868–876. [PubMed: 16644758]
45. Khaw, BA. Antibodies: considerations for in vitro and in vivo applicationseds. In: Khaw, BA.; Narula, J.; Strauss, HW., editors. Monoclonal Antibodies in Cardiovascular Diseases. Philadelphia, PA: Lea & Febiger, a Waverly Co; 1994. p. 1-12.
46. Khaw BA, Gold HK, Yasuda T, et al. Scintigraphic quantification of myocardial necrosis in patients after intravenous injection of myosin-specific antibody. Circulation. 1986; 74:501–508. [PubMed: 3017604]
47. Khaw BA, Yasuda T, Gold HK, et al. Acute myocardial infarct imaging with indium-111-labeled monoclonal antimyosin Fab. J Nucl Med. 1987; 28:1671–1678. [PubMed: 3668661]
48. Patil, V.; Pincus, D.; Keyur, G., et al. Molecular imaging of lung metastatic melanoma with bispecific antibody and Tc-99m labeled polymers: signal amplification allows visualization of very small lesion. Paper presented at: World Molecular Imaging Congress; September 10–13, 2008; Nice, France.
49. Gada, K.; Patil, V.; Khaw, B., et al. Enhanced targeted tumorotoxicity and reduced cardiotoxicity with bispecific antibody-polymer-prodrug complexes: in vitro studies with BT-20 human breast carcinoma and embryonic cardiocytes. Poster presented at: 35th Annual Meeting & Exposition of the Controlled Release Society; July 13–16, 2008; New York, NY.
50. Vasey PA, Kaye SB, Morrison R, et al. Phase I clinical and pharmacokinetic study of PK1 [*N*-(2-hydroxypropyl)methacrylamide copolymer doxorubicin]: first member of a new class of chemotherapeutic agents-drug-polymer conjugates. Cancer Research Campaign Phase I/II Committee. Clin Cancer Res. 1999; 5:83–94. [PubMed: 9918206]
51. Matsumura Y, Maeda H. A new concept for macromolecular therapeutics in cancer chemotherapy: mechanism of tumoritropic accumulation of proteins and the antitumor agent SMANCS. Cancer Res. 1986; 46:6387–6392. [PubMed: 2946403]
52. Almutairi A, Rossin R, Shokeen M, et al. Biodegradable dendritic positronemitting nanoprobes for the noninvasive imaging of angiogenesis. Proc Natl Acad Sci USA. 2009; 106:685–690. [PubMed: 19129498]
53. Torchilin VP. Micellar nanocarriers: pharmaceutical perspectives. Pharm Res. 2007; 24:1–16. [PubMed: 17109211]
54. ElBayoumi TA, Torchilin VP. Tumor-targeted nanomedicines: enhanced antitumor efficacy in vivo of doxorubicin-loaded, long-circulating liposomes modified with cancer-specific monoclonal antibody. Clin Cancer Res. 2009; 15:1973–1980. [PubMed: 19276264]
55. Park JS, Na K, Woo DG, et al. Non-viral gene delivery of DNA polyplexed with nanoparticles transfected into human mesenchymal stem cells. Biomaterials. 2010; 31:124–132. [PubMed: 19818490]
56. Glickson JD, Lund-Katz S, Zhou R, et al. Lipoprotein nanoplatform for targeted delivery of diagnostic and therapeutic agents. Adv Exp Med Biol. 2009; 645:227–239. [PubMed: 19227476]

57. Nahrendorf M, Zhang H, Hembrador S, et al. Nanoparticle PET-CT imaging of macrophages in inflammatory atherosclerosis. Circulation. 2008; 117:379–387. [PubMed: 18158358]
58. Prato M, Kostarelos K, Bianco A. Functionalized carbon nanotubes in drug design and discovery. Acc Chem Res. 2008; 41:60–68. [PubMed: 17867649]
59. Jeon SI, Andrade JD. Protein-surface interactions in the presence of polyethylene oxide. II. Effect of protein size. J Colloid Interface Sci. 1991; 142:159–166.
60. Jeon SI, Lee JH, Andrade JD, De Gennes PG. Protein-surface interactions in the presence of polyethylene oxide. I. Simplified theory. J Colloid Interface Sci. 1991; 142:149–158.
61. Sun G, Hagooly A, Xu J, et al. Facile, efficient approach to accomplish tunable chemistries and variable biodistributions for shell cross-linked nanoparticles. Biomacromolecules. 2008; 9:1997–2006. [PubMed: 18510359]
62. Sun G, Xu J, Hagooly A, et al. Strategies for optimized radiolabeling of nanoparticles for in vivo PET imaging. Adv Mater. 2007; 19:3157–3162.
63. Devaraj NK, Keliher EJ, Thurber GM, Nahrendorf M, Weissleder R. F-18-labeled nanoparticles for in vivo PET-CT imaging. Bioconjug Chem. 2009; 20:397–401. [PubMed: 19138113]
64. Lee HY, Li Z, Chen K, et al. PET/MRI dual-modality tumor imaging using arginine-glycine-aspartic (RGD)-conjugated radiolabeled iron oxide nanoparticles. J Nucl Med. 2008; 49:1371–1379. [PubMed: 18632815]
65. Hood JD, Cheresh DA. Role of integrins in cell invasion and migration. Nat Rev Cancer. 2002; 2:91–100. [PubMed: 12635172]
66. Pressly ED, Rossin R, Hagooly A, et al. Structural effects on the biodistribution and positron emission tomography (PET) imaging of well-defined ^{64}Cu-labeled nanoparticles comprised of amphiphilic block graft copolymers. Biomacromolecules. 2007; 8:3126–3134. [PubMed: 17880180]

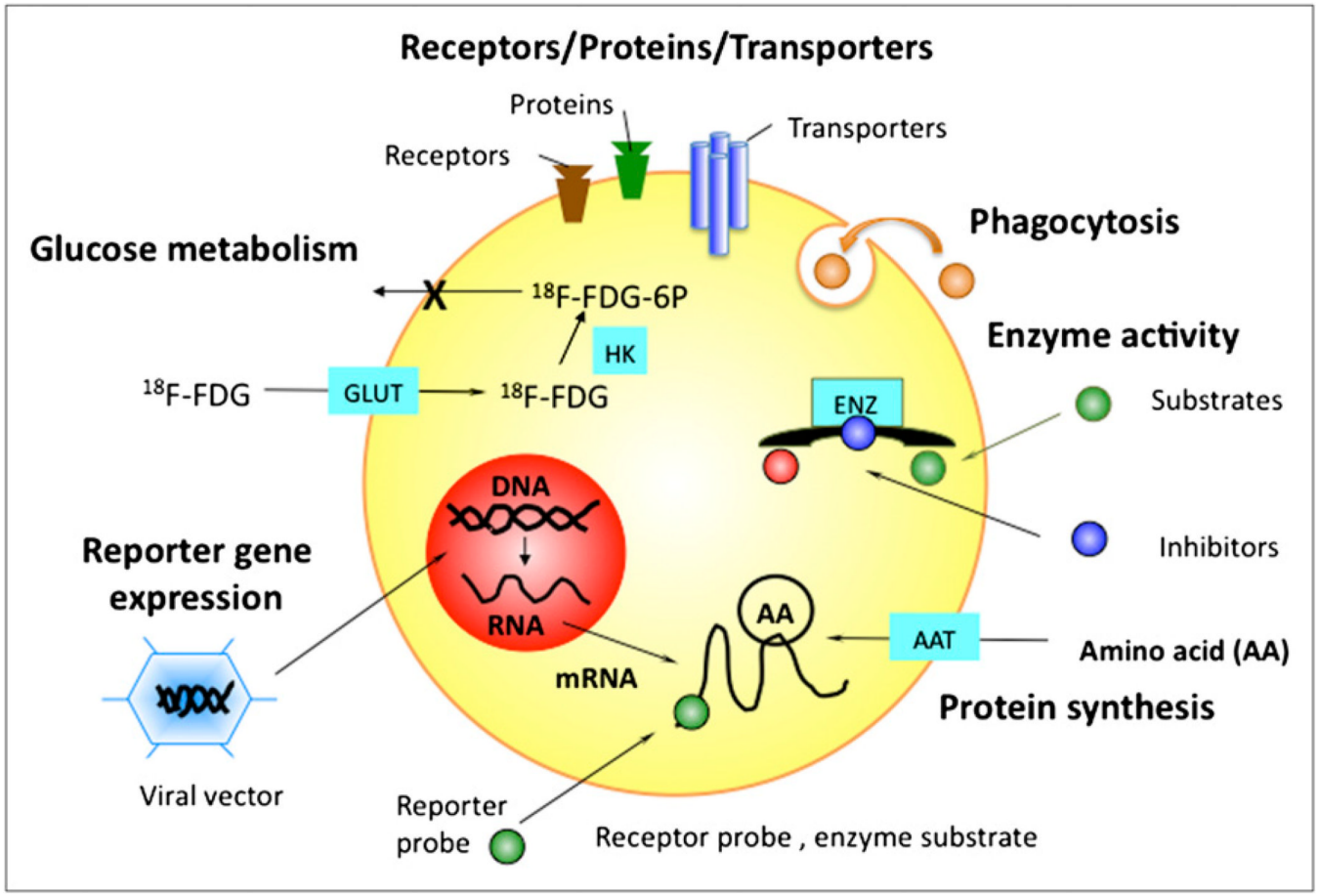

FIGURE 1.
Examples of cellular targets for molecular imaging agents. AAT = amino acid transporter; ENZ = enzyme; GLUT = glucose transporter; HK = hexokinase; 6P = 6-phosphate.

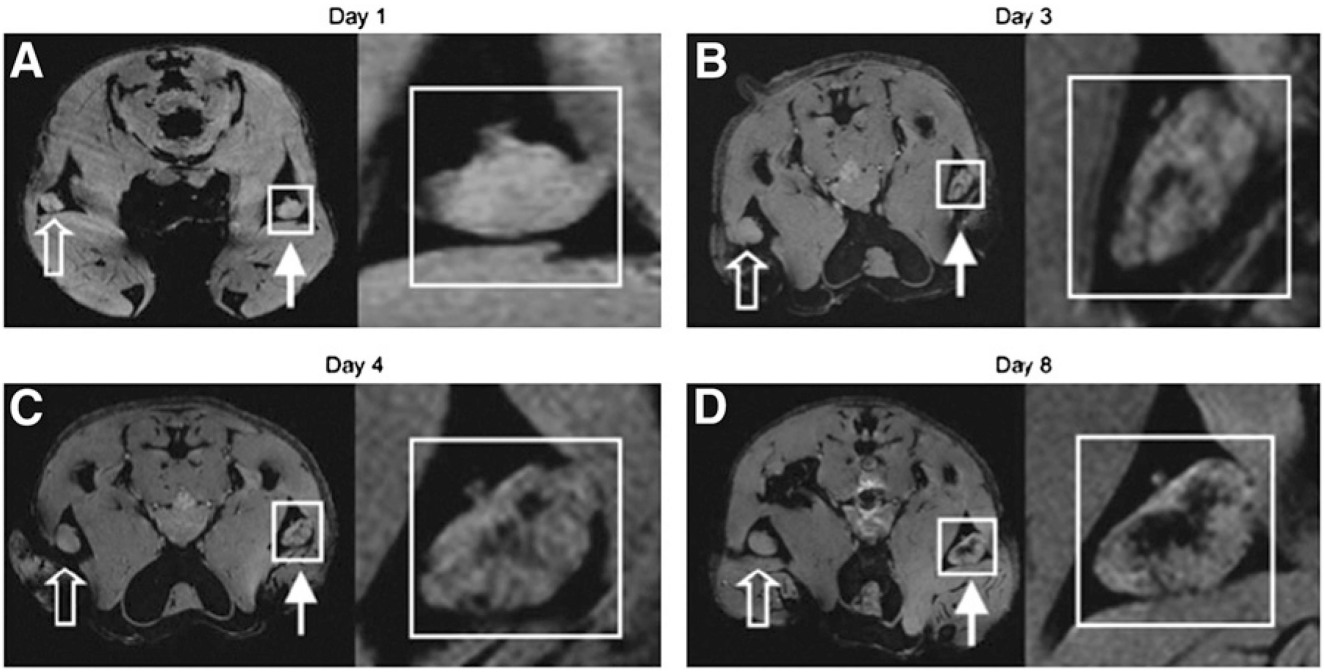

FIGURE 2.

In vivo MRI monitoring of trafficking of dendritic cells that have taken up SPIOs in vivo after intradermal injection of labeled granulocyte–macrophage colony-stimulating (GM CSF) tumor cell vaccine into footpads of mice. For each day, magnifications of insets in A, B, C, and D are shown at right. Open arrows represent draining popliteal lymph nodes (LNs) for footpads receiving unlabeled GM CSF vaccine. Closed arrows represent draining popliteal LNs for footpads receiving SPIO-labeled GM CSF vaccine. On multigradient-echo images, SPIO-containing LNs have decreased signal intensity. (A) On day 1, popliteal LNs show no evidence of hypointensity. (B) On day 3, decreased signal intensity becomes apparent in LN corresponding to popliteal LN for SPIO-labeled vaccine. (C and D) On day 4 (C) and day 8 (D), respectively, signal decrease persists and then actually increases in popliteal LNs. Images are representative of 3 independent experiments with 5 mice each. (Reprinted with permission of (4).

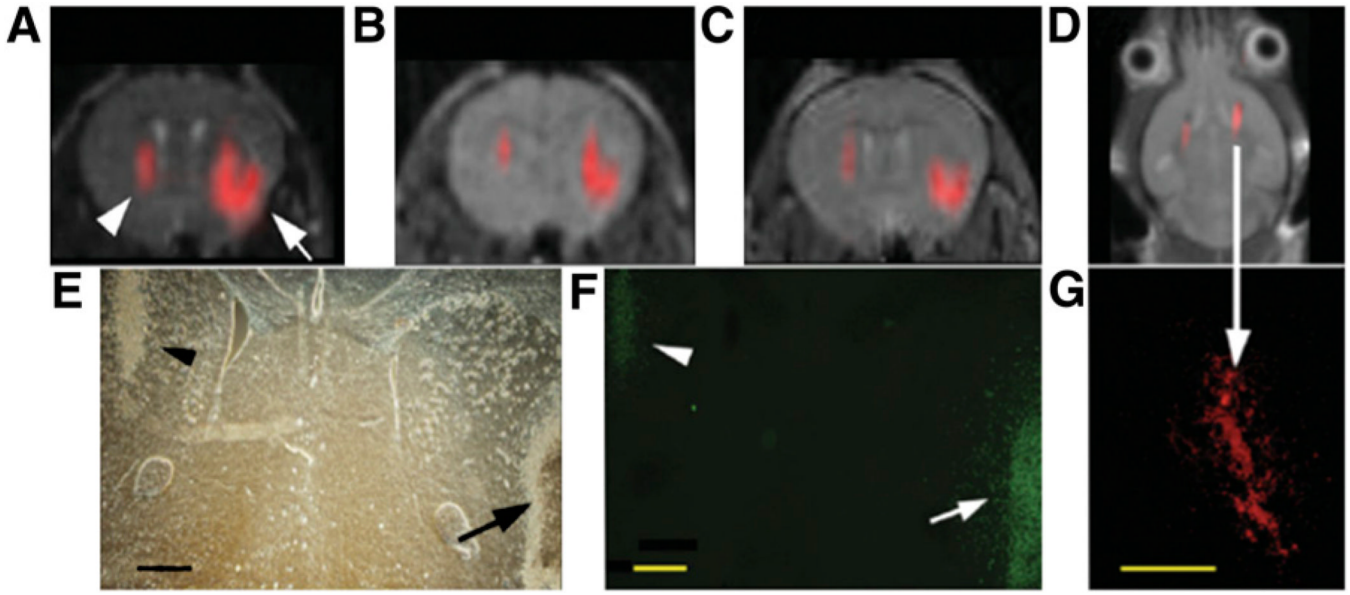

FIGURE 3.

In vivo MRI of transplanted C17.2 neural stem cells, with ^{19}F signal superimposed on ^{1}H MR images. (A–C) MR images at 1 h (A), 3 d (B), and 7 d (C) after injection of 4×10^4 (left hemisphere, arrowhead in A) or 3×10^5 (right hemisphere, arrow in A) cationic perfluoro crown ether (PFCE)–labeled cells. (E and F) Corresponding histopathology determined with phase-contrast microscopy (E) and anti–β-galactosidase immunohistochemistry (F) at day 7 shows that implanted cells remain viable and continue to produce marker enzyme. Arrow in F indicates cells migrating from injection site into brain parenchyma. (D) MR image of different animal at 14 d after injection of 4×10^5 C17.2 cells into both hemispheres shows persistence of ^{19}F signal for 2 wk. (G) Corresponding histopathology shows rhodamine fluorescence from PFCE-labeled cells colocalizing with ^{19}F signal. Bars = 500 μm. (Reprinted with permission of (15).

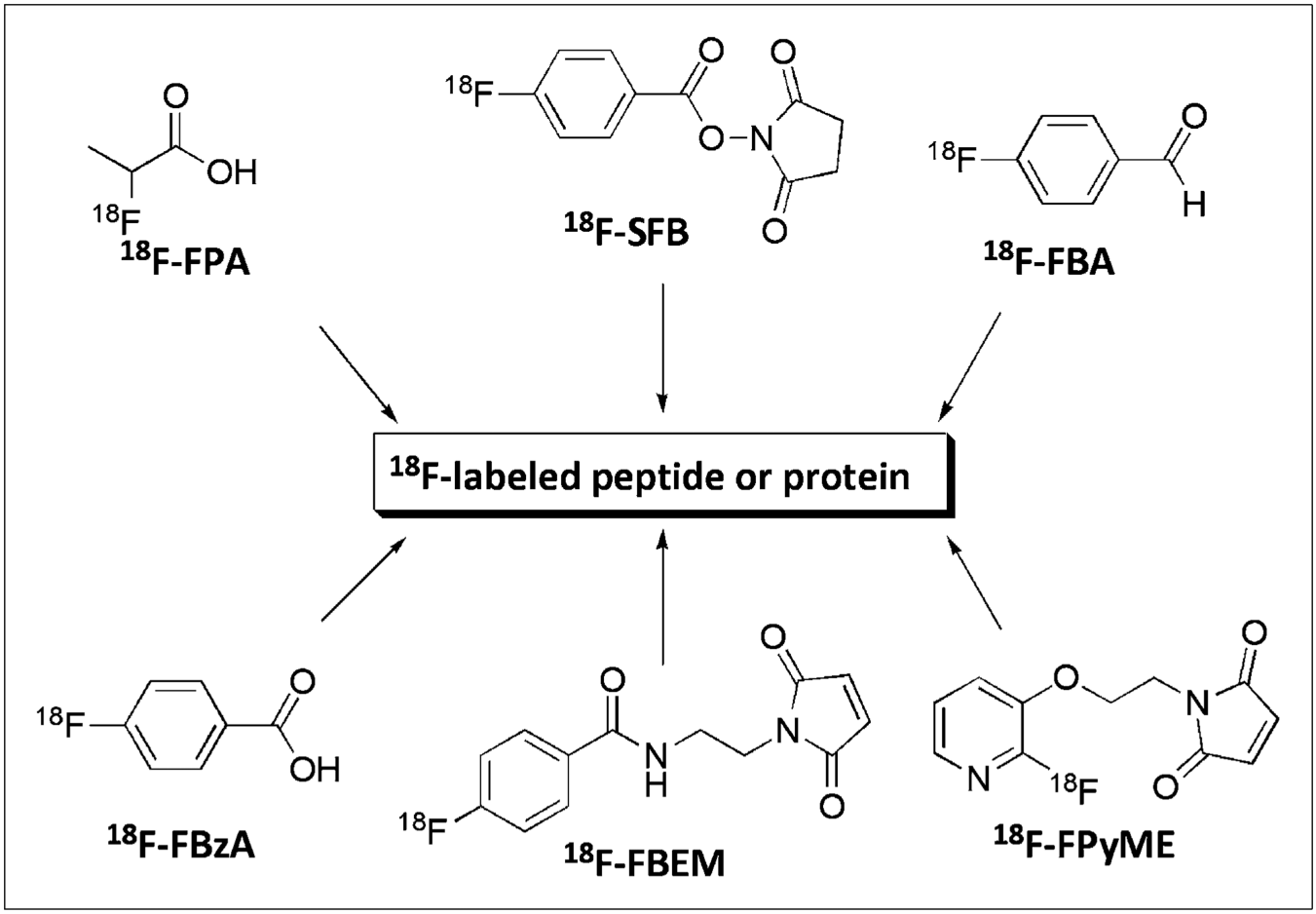

FIGURE 4.

Prosthetic groups for ^{18}F labeling of peptides and proteins. FBA = fluorobenzaldehyde; FBEM = fluorobenzamido–ethylmaleimide; FBzA = fluorobenzoic acid; FPA = fluoropropionic acid; FpyME = fluoropyridinyloxy–propylmaleimide; SFB = succinimidyl fluorobenzoate.

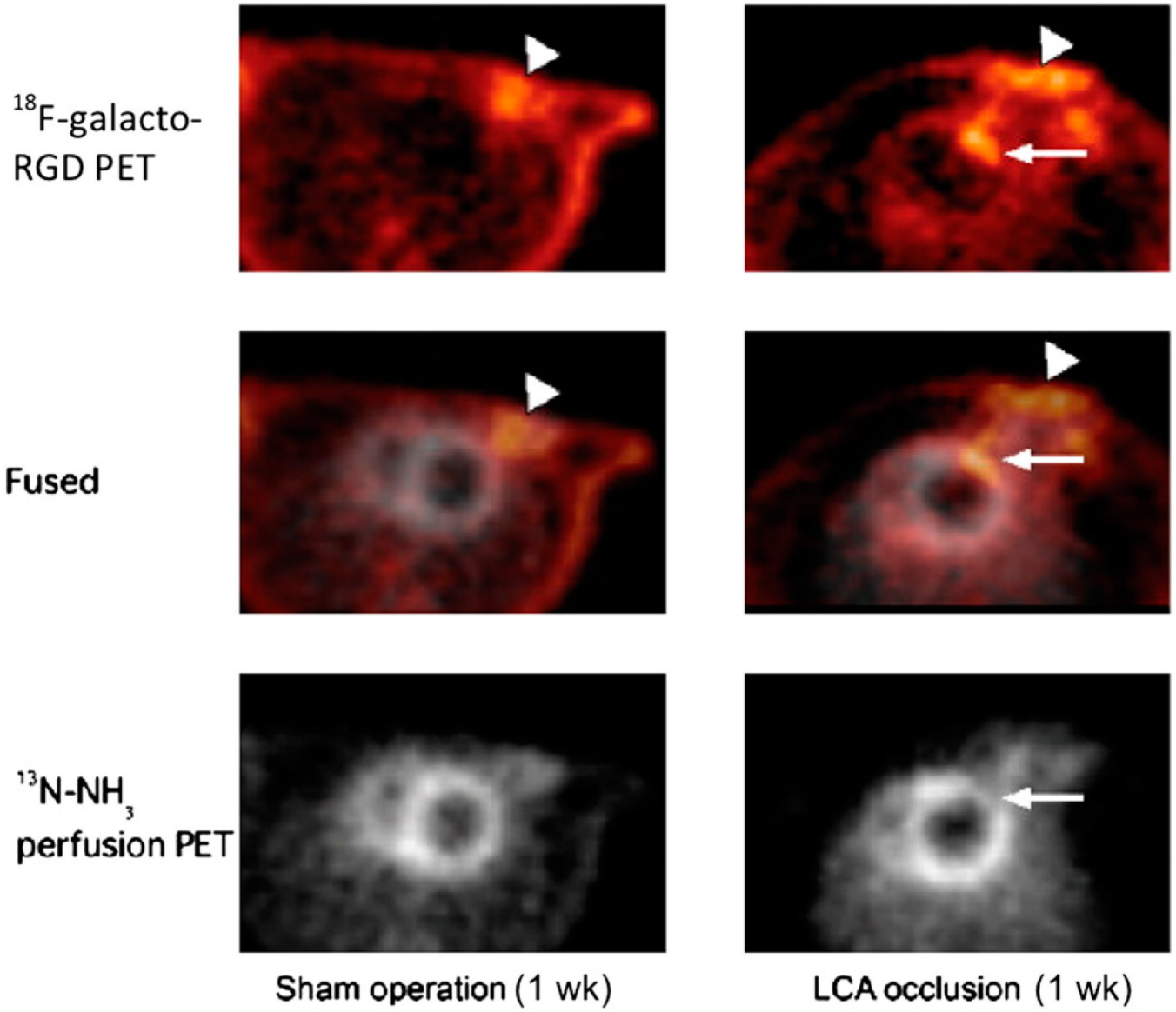

FIGURE 5.
In vivo PET images of ^{18}F-galacto-RGD uptake (top), ^{13}N-NH3 perfusion (bottom), and their fusion (middle) in transverse views of rat heart without coronary occlusion (sham operation, left) and rat heart with 20 min of coronary occlusion 1 wk after reperfusion (right). Tracer accumulation is visible in chest wall at surgical incision area in both rats (arrowheads), but focal ^{18}F-galacto-RGD uptake in myocardium is observed only after coronary occlusion (arrows). LCA = left anterior descending coronary artery. (Reprinted with permission of (27).

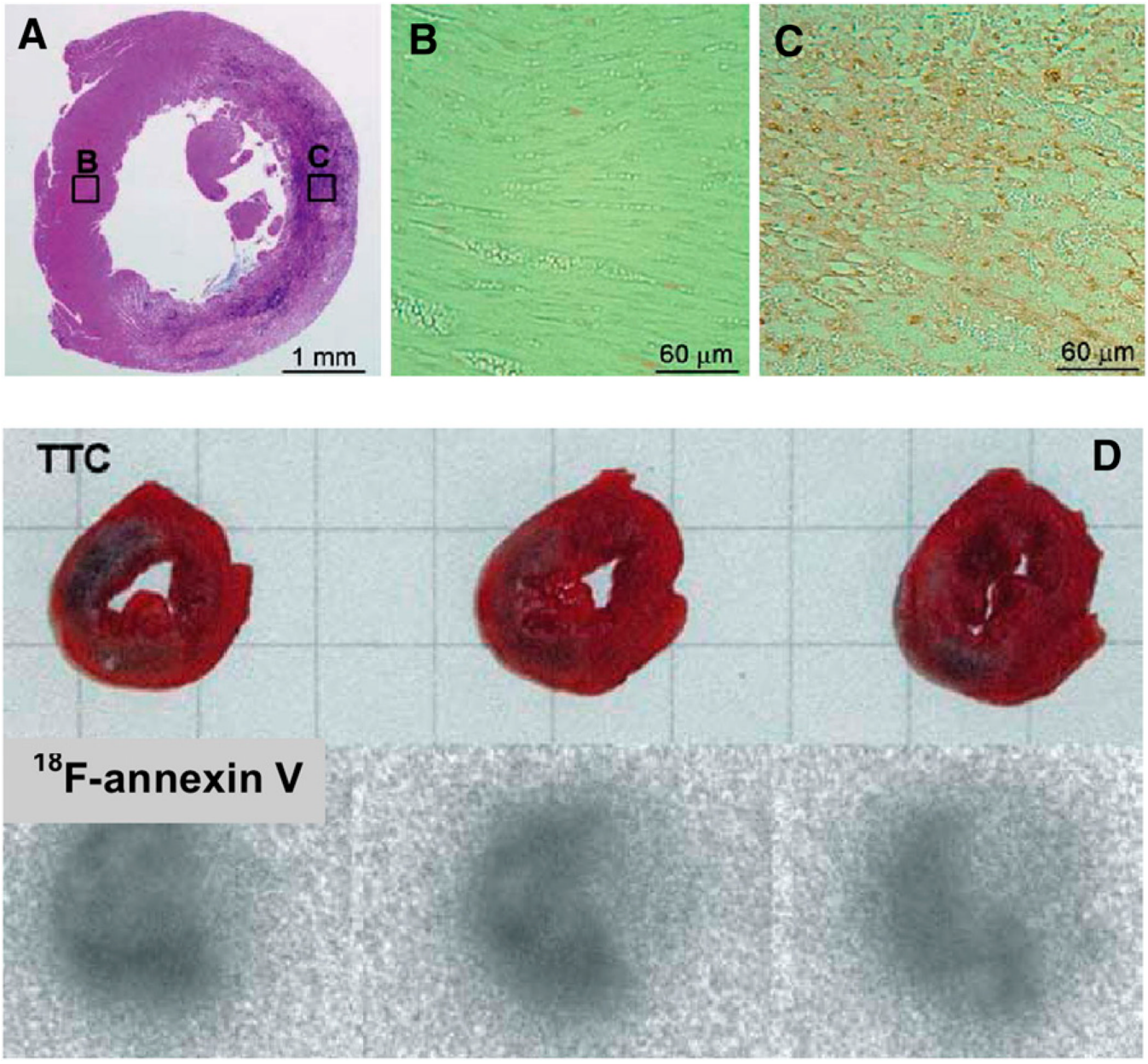

FIGURE 6.

(A–C) Typical results of hematoxylin and eosin staining of left ventricle at 24 h after ischemia (A) and detection of apoptosis in regions shown in boxes B and C (B and C). (D) Typical infarction in left ventricle at 24 h after ischemia (2,3,5-triphenyltetrazolium chloride [TTC] stain) and accumulation of ^{18}F-annexin V. (Reprinted with permission of (28).

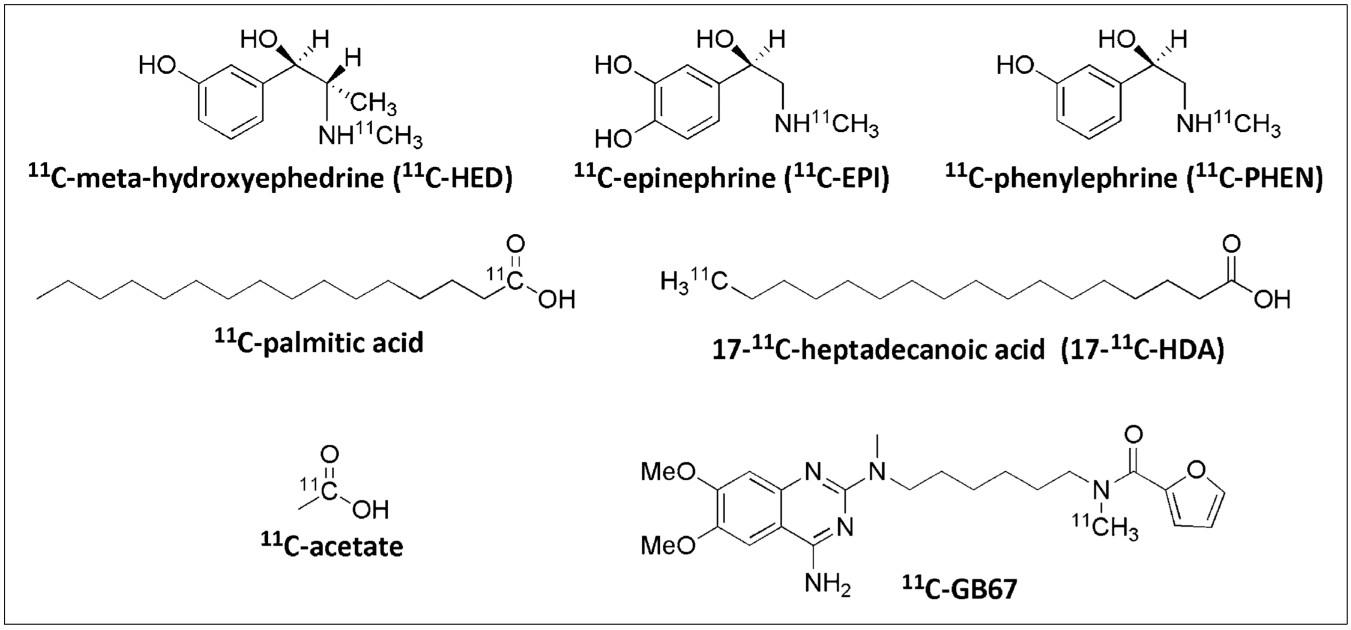

FIGURE 7.
Selected ^{11}C PET radiotracers for cardiac imaging.

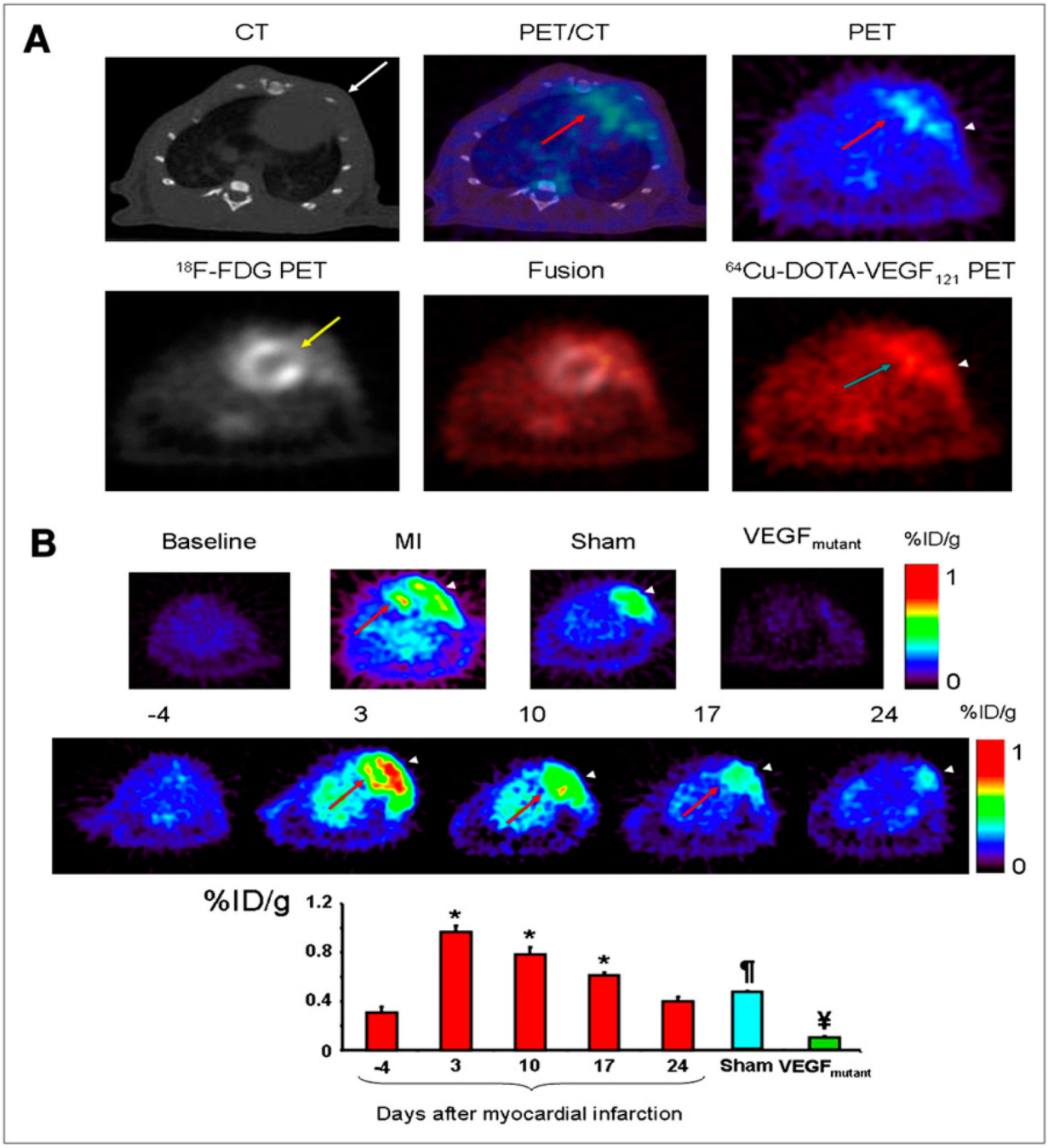

FIGURE 8.

(A) Myocardial origin of ^{64}Cu-DOTA-VEGF$_{121}$ PET signal after MI. (Top) Representative coregistered images from micro-CT (left), PET (right), and fused PET/CT (middle) of animal with MI. (Bottom) Representative ^{64}Cu-DOTA-VEGF$_{121}$ image (left), ^{18}F-FDG image (right), and ^{64}Cu-DOTA-VEGF$_{121}$–^{18}F-FDG fused image (middle). (B) Time-dependent uptake of ^{64}Cu-DOTA-VEGF$_{121}$. Arrowhead = area of surgical wound; red arrow = anterolateral myocardium; white arrow = intercostal muscle layer; yellow arrow = ligated coronary artery. *$P < 0.05$ compared with baseline. ¶$P < 0.05$ compared with VEGFmutant and ^{64}Cu-DOTA-VEGF121. ¥$P < 0.05$ compared with sham and ^{64}Cu-DOTA-VEGF121.

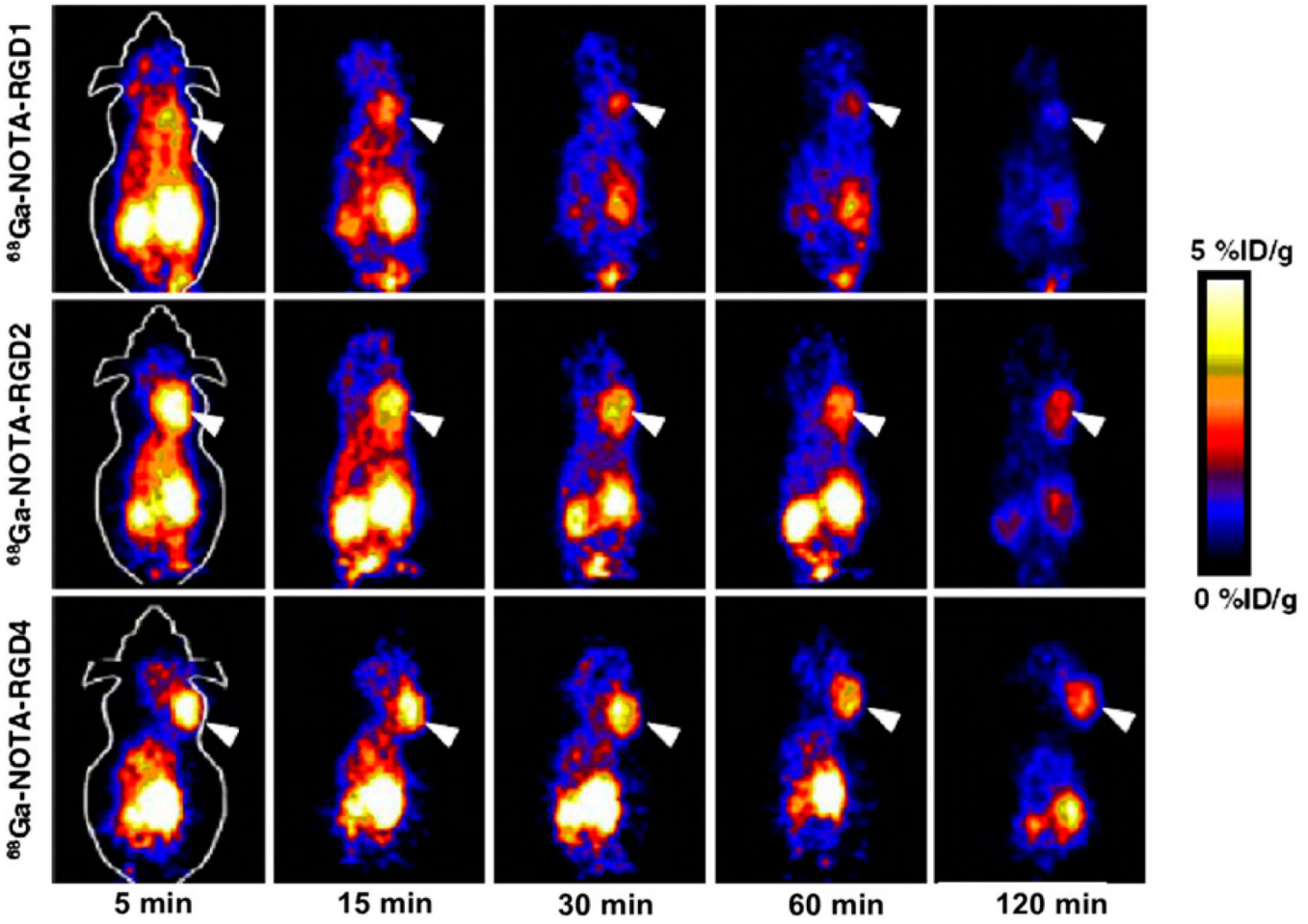

FIGURE 9.

Decay-corrected whole-body coronal small-animal PET images of athymic female nude mice bearing U87MG tumors from 1-h dynamic scan and static scan at 2 h after injection of ^{68}Ga-NOTA-RGD1, ^{68}Ga-NOTA-RGD2, and ^{68}Ga-NOTA-RGD4 (3.7 MBq/mouse). Tumors are indicated by arrowheads.

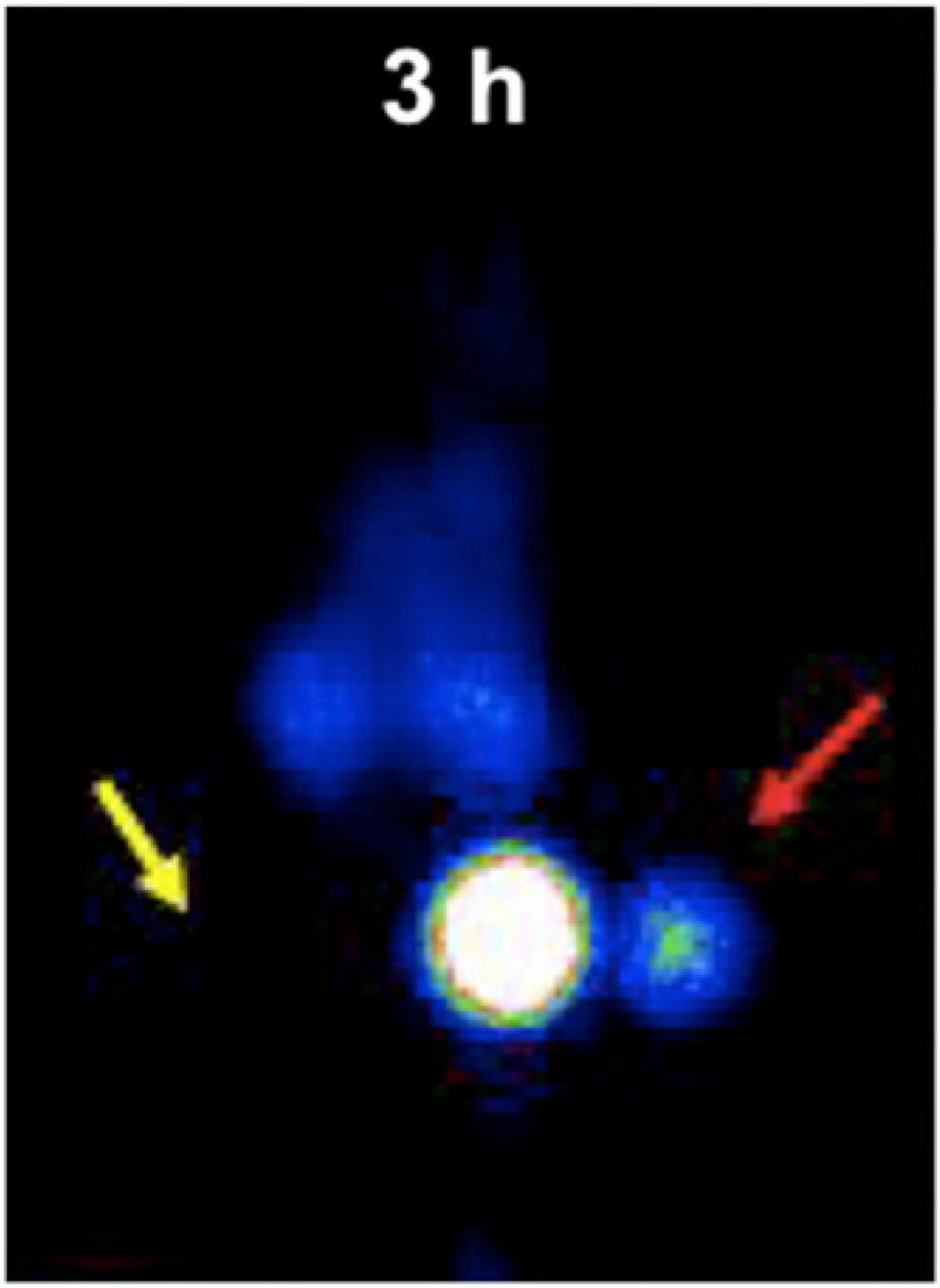

FIGURE 10.

Anteroposterior γ-image of mouse with experimental atherosclerotic lesion in left femoral artery (red arrow) and contralateral sham-treated right femoral region (yellow arrow) at 3 h after injection of ^{99m}Tc-labeled DTPA-conjugated succinylated polylysine polymer. Inject ion of polymer followed pretargeting with bispecific antibody Z2D3 F(ab′)$_2$– anti-DTPA F(ab′)$_2$ (44). Lesion in left femoral artery was about 2.5 mg, as determined by immunohistochemical staining.

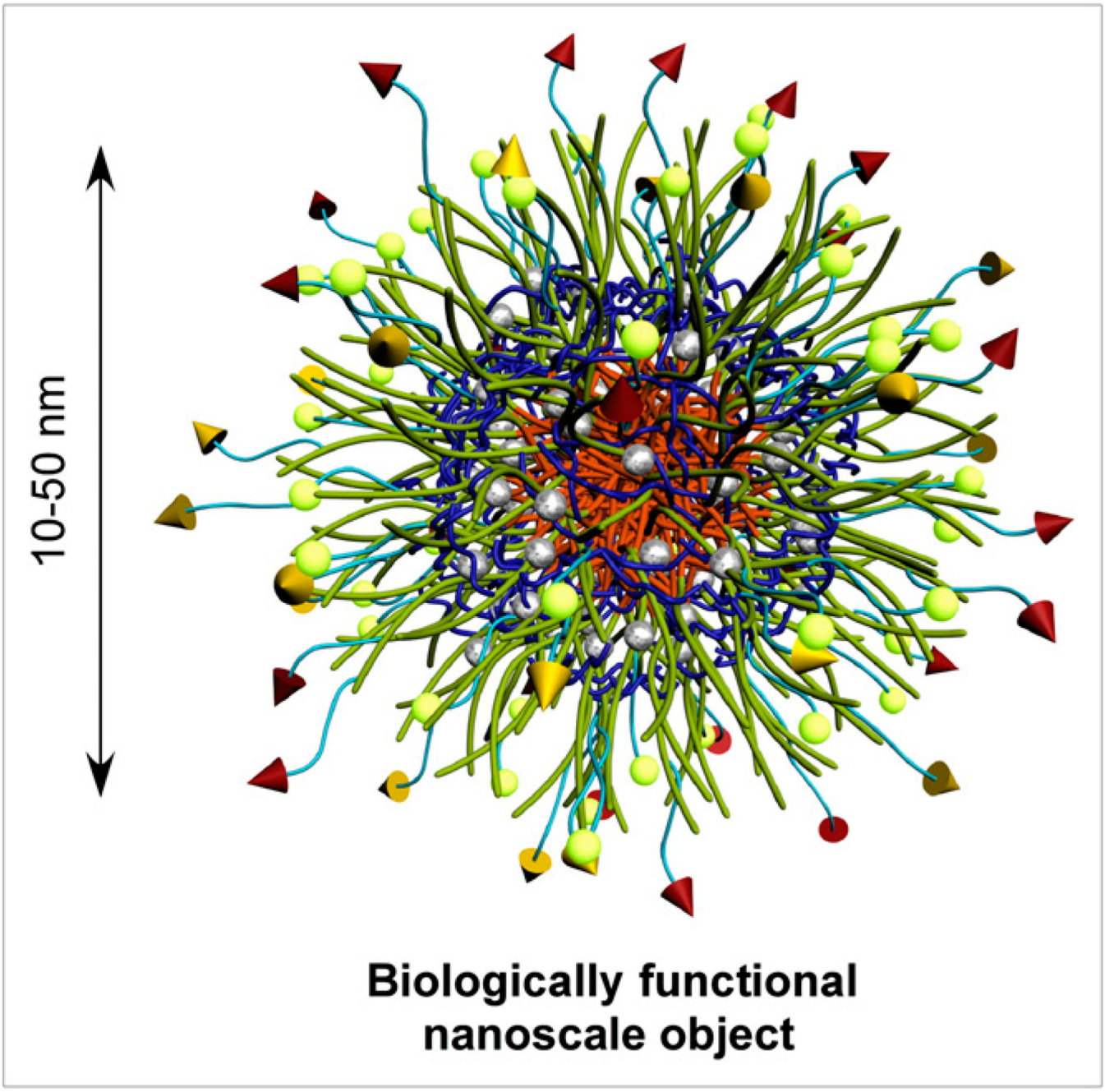

FIGURE 11.
Schematic illustration of general core–shell morphology of multifunctional spheric nanoparticle.

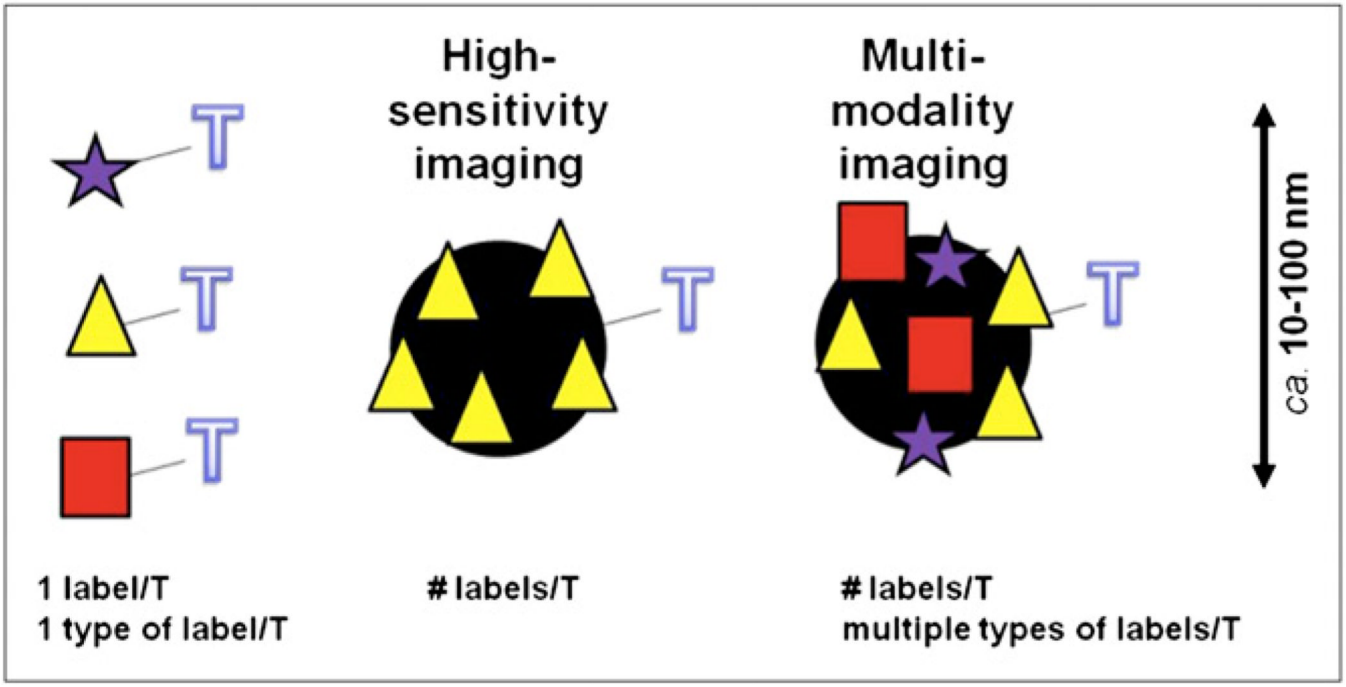

FIGURE 12.
Nanomaterials offering potential for high-sensitivity imaging and multimodality imaging relative to singly labeled (☆,Δ,☐) targeting ligands (T).

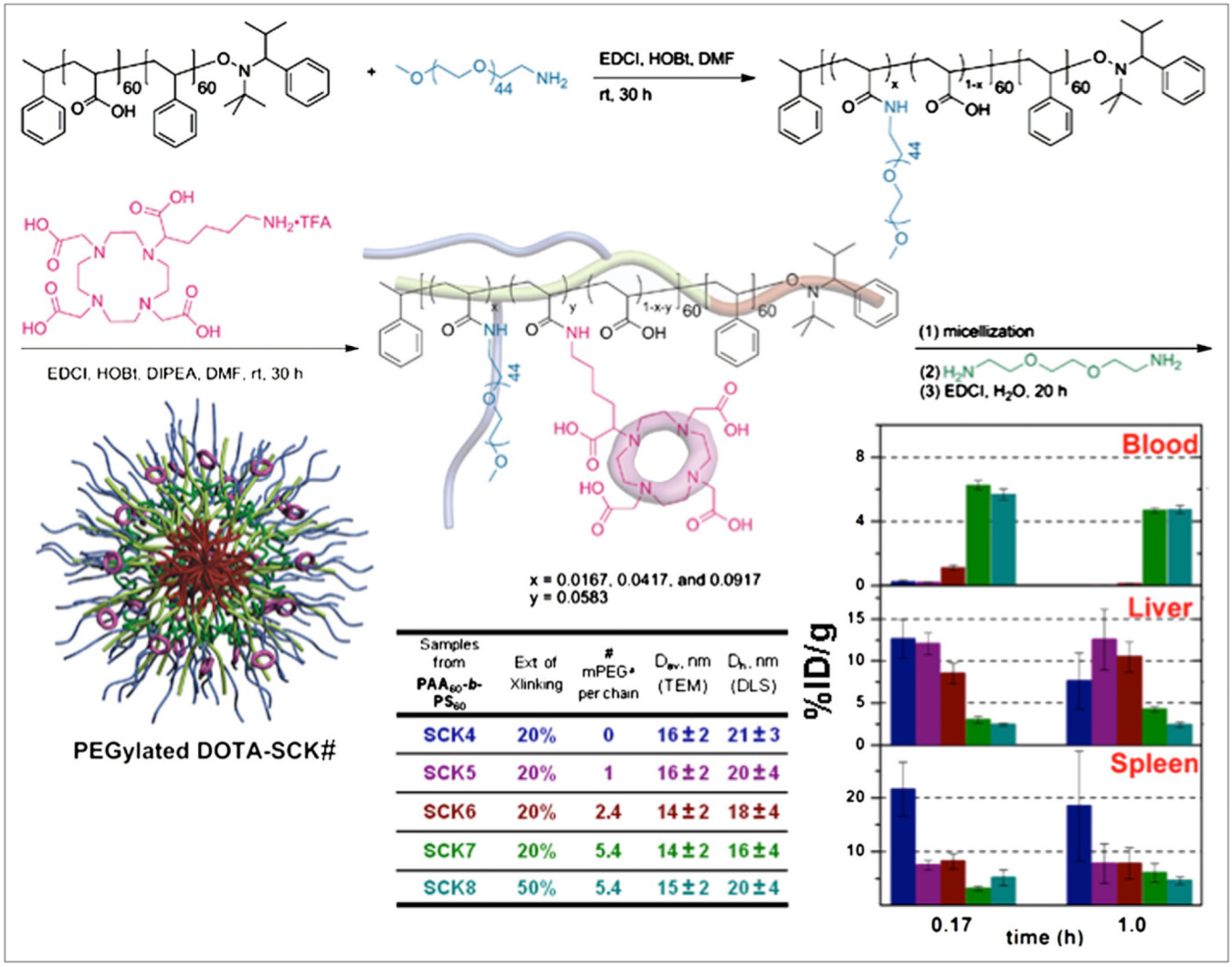

Samples from PAA_{60}-b-PS_{60}	Ext of Xlinking	# mPEG[a] per chain	D_{ev}, nm (TEM)	D_h, nm (DLS)
SCK4	20%	0	16±2	21±3
SCK5	20%	1	16±2	20±4
SCK6	20%	2.4	14±2	18±4
SCK7	20%	5.4	14±2	16±4
SCK8	50%	5.4	15±2	20±4

FIGURE 13.

Pegylated DOTA–shell cross-linked knedel-like nanoparticles (SCKs) originate from amphiphilic block copolymers to which are coupled desired numbers of PEG and DOTA units, so that final assembled nanoparticle has well-defined structure and quantifiable PEG and DOTA levels. Surface coverage by PEG (parameters described in table) alters biodistribution significantly. PEGylated DOTA-SCK# label under nanoparticle structure corresponds to compounds listed in table, and color code in table links nanoparticles to biodistribution bar graphs at right.

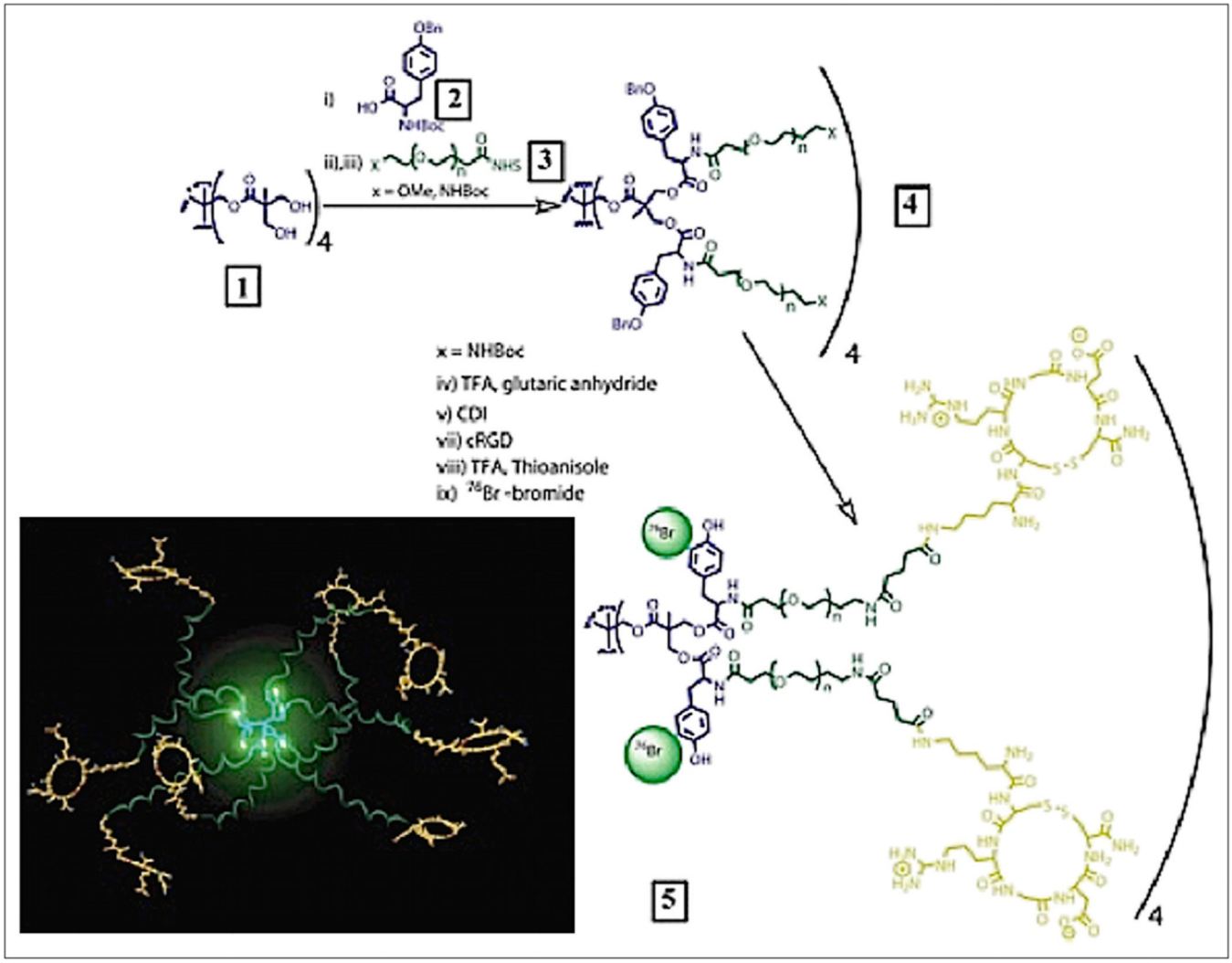

FIGURE 14.
Preparation of PET nanoprobes targeted to $\alpha_v\beta_3$-integrin.

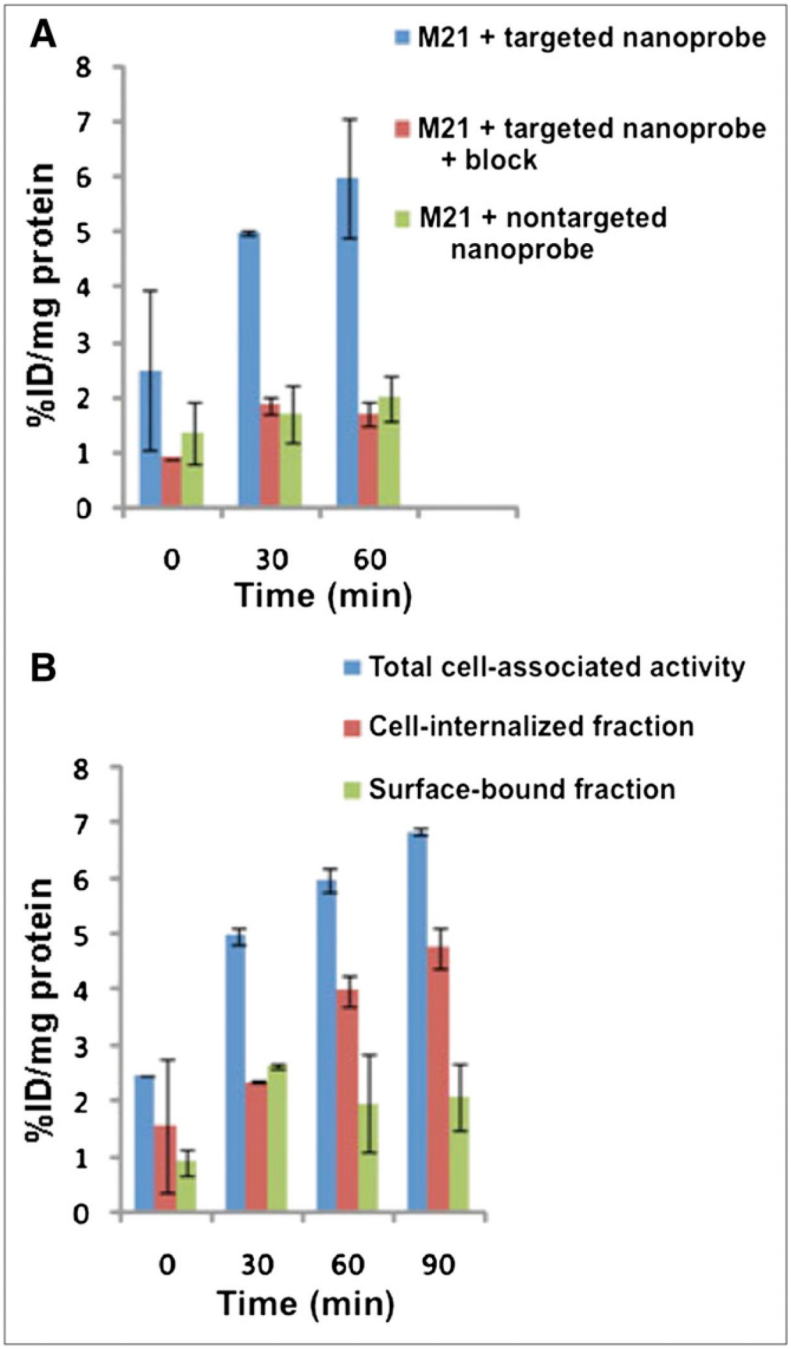

FIGURE 15.

Cell uptake studies. (A) Percentages of total cell-associated fraction, cell-internalized fraction, and surface-bound fraction for targeted nanoprobe in $\alpha_v\beta_3$-integrin–positive M21 cells. (B) Percentages of cell-internalized fraction for targeted nanoprobe in absence and presence of block and nontargeted nanoprobe in $\alpha_v\beta_3$-integrin– positive M21 cells. All values were normalized to protein content per well. Total cell-associated fraction represents sum of cell-internalized fraction and surface-bound fraction. %ID/mg protein = percentage injected or administered dose per milligram of protein.

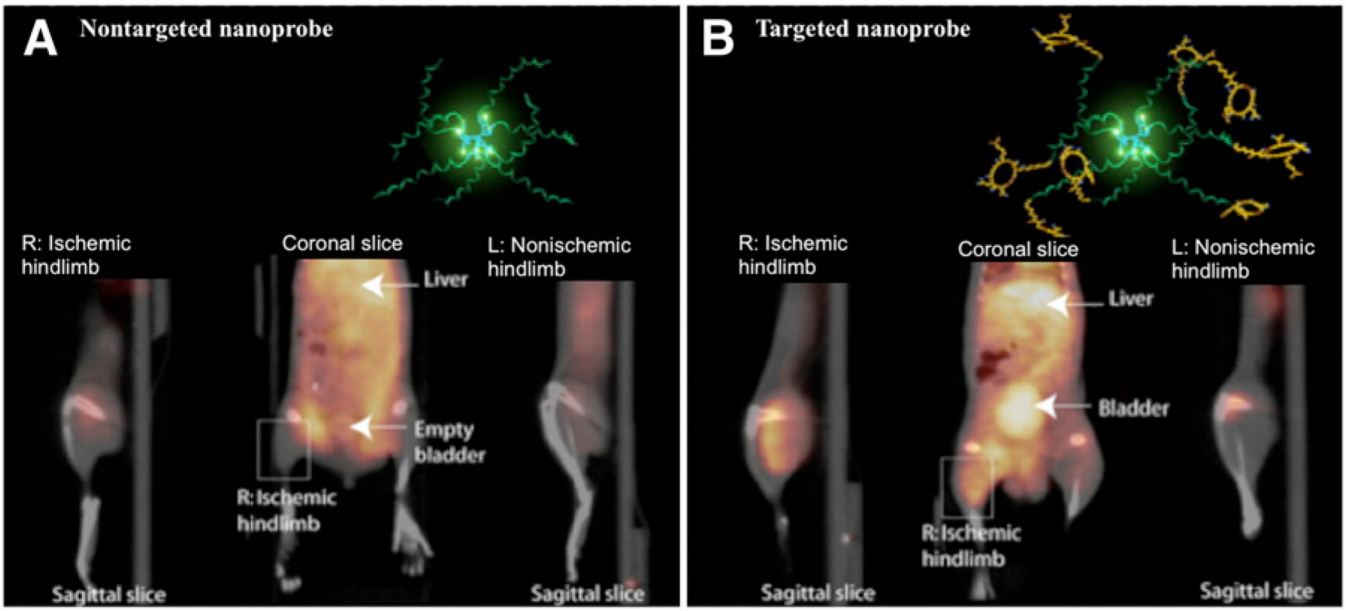

FIGURE 16.

Noninvasive PET/CT images of angiogenesis induced by hind limb ischemia in murine model. (A) Nontargeted dendritic nanoprobes (bottom, middle). (B) Uptake of $\alpha_v\beta_3$-integrin–targeted dendritic nanoprobes was higher in ischemic hind limb (left) than in control hind limb (right).

TABLE 1

Positron-Emitting Radionuclides for PET

Radionuclide	Reaction	Half-life
Conventional		
^{15}O	$^{14}N(d,n)^{15}O$	2.04 min
^{13}N	$^{16}O(p,n)^{13}N$	9.97 min
^{11}C	$^{14}N(p,n)^{11}C$	20.4 min
^{18}F	$^{18}O(p,n)^{18}F$	109.8 min
Nonconventional		
^{60}Cu	$^{60}Ni(p,n)^{60}Cu$	23.7 min
^{94m}Tc	$^{94}Mo(p,n)^{94m}Tc$	52 min
^{66}Ga	$^{66}Zn(p,n)^{66}Ga$	9.5 h
^{64}Cu	$^{64}Ni(p,n)^{64}Cu$	12.8 h
^{86}Y	$^{86}Sr(p,n)^{86}Y$	14.7 h
^{76}Br	$^{76}Se(p,n)^{76}Br$	16.2 h
^{89}Zr	$^{89}Y(p,n)^{89}Zr$	78 h
^{124}I	$^{124}Te(p,n)^{124}I$	4.2 d
^{68}Ga	$^{68}Ge/^{68}Ga$	68 min
^{62}Cu	$^{62}Zn/^{62}Cu$	9.74 min